Ice, wind, and water: Synoptic-scale controls of circulation in the Chukchi Sea

Bridget Ovall[a,b], Robert S. Pickart[a], Peigen Lin[a], Phyllis Stabeno[c], Thomas Weingartner[d], Motoyo Itoh[e], Takashi Kikuchi[e], Elizabeth Dobbins[d], Shaun Bell[c,f]

[a] Woods Hole Oceanographic Institution, Woods Hole, MA 02543, USA.

[b] present address: Department of Marine and Coastal Sciences, Rutgers University, New Brunswick, NJ 08901, USA

[c] Pacific Marine Environmental Laboratory, National Oceanic and Atmospheric Administration, Seattle, WA, USA

[d] College of Fisheries and Ocean Sciences, University of Alaska, Fairbanks, AK 99775, USA

[e] Institute of Observational Research for Global Change, Japan Agency for Marine-Earth Science and Technology, Yokosuka, Japan

[f] Joint Institute for the Study of the Atmosphere and Oceans, University of Washington, Box 354235, Seattle, WA 98195-4235, USA

Corresponding author: B. Ovall (bovall@marine.rutgers.edu)

19   **Abstract**

20   A composite dataset of 27 moorings across the Chukchi Sea and Bering Strait in 2013-14,

21   along with satellite sea ice concentration data, weather station data, and atmospheric reanalysis

22   fields, are used to explore the relationship between the circulation, ice cover, and wind forcing.

23   We find a clear relationship between northeasterly winds along the northwest coast of Alaska

24   and reversed flow along the length of Barrow Canyon and at a mooring site ~100 km upstream

25   on the northeast shelf. Atlantic Water is frequently upwelled into the canyon during the fall and

26   winter, but is only able to reach the head of Barrow Canyon after a series of long upwelling

27   events. A pair of empirical orthogonal function (EOF) analyses of ice cover reveal the

28   importance of inflow pathways on the pattern of freeze-up and melt-back, and shed light on the

29   relative influence of sensible heat and wind forcing on polynya formation. An EOF analysis of

30   25 mooring velocity records reveals a dominant pattern of circulation with coherent flow across

31   the shelf, and a secondary pattern of opposing flow between Barrow Canyon and Bering Strait.

32   These are related to variations in the regional wind field.

1. Introduction

As one of the most productive areas in the global ocean (Grebmeier et al., 2006) and as part of a region currently experiencing a significant decline in sea ice cover (Frey et al., 2015), a better understanding of physical processes in the Chukchi Sea is critical to our understanding of the changing ecosystem dynamics. Timing of melt-back in sea ice controls the seasonal transition from ice algae to phytoplankton as primary producers. An earlier melt-back could shift the ecosystem from a benthic-dominated to a pelagic-dominated regime (Grebmeier et al., 2006; Moore & Stabeno, 2015). Through brine rejection during ice production, the frequency, extent, and duration of polynyas influence the density of winter waters and the depth to which they ventilate the western Arctic (Itoh et al., 2012; Weingartner et al., 1998). The resulting deep convection homogenizes the water column and can resuspend nutrients from the sea floor (Pacini et al., 2019; Pickart et al., 2016). Circulation patterns then control the distribution of nutrients throughout the Chukchi Sea (Pickart et al., 2016), which in turn influences the location and strength of the phytoplankton blooms.

In recent years, a general understanding of the circulation across the Chukchi Sea and regions of likely exchange with the Arctic Basin has emerged (Fig. 1). Flow through Bering Strait is primarily northward, with a higher transport in the summer months (Woodgate et al., 2005a). Northward flow continues across the Chukchi Sea along three major, topographically steered pathways. The coastal pathway, known as the Alaskan Coastal Current (ACC) in the summer, is the most direct route and follows the Alaska coastline across the shelf, draining through Barrow Canyon. The Central Channel pathway flows northward from Bering Strait and subsequently divides into several branches, each eventually turning eastward towards Barrow Canyon (e.g. Pickart et al., 2016). The western pathway is the most circuitous. A portion of this water flows westward through Long Strait into the East Siberian Sea (Woodgate et al., 2005). The rest flows around the west side of Herald Shoal into Herald Canyon. A bifurcation just north of the canyon diverts some of the flow eastward, which joins the Central Channel pathway near Hanna Shoal. Thus, a large portion of the Bering Strait inflow ends up flowing through Barrow Canyon. However, transit times vary greatly by pathway, ranging from as little as 2-3 months in the coastal pathway (Tian et al., 2021; Weingartner et al., 1998) to 6-8 months for the northernmost branch of the Central Channel pathway (Spall, 2007). Additionally, each pathway experiences intermittent flow reversals associated with local winds, which increase the transit

64   times.

65   Several studies have explored the connection between local wind forcing and flow

66   reversals within Barrow Canyon (e.g., Itoh et al., 2013; Weingartner et al., 2017; Lin et al.,

67   2019a; Pisareva et al., 2019). Northeasterly wind along the northwest coast of Alaska drives

68   offshore Ekman transport, which in turn leads to upwelling in the canyon. Such wind events are

69   frequent, especially in fall and winter. Continental shelf waves are also thought to play a role in

70   upwelling in this region (Aagaard & Roach, 1990; Danielson et al., 2014). Episodes of upwelling

71   have been known to draw warm, salty Atlantic Water from the deep Arctic Basin, sometimes far

72   onto the shelf (Bourke & Paquette, 1976; Ladd et al., 2016).
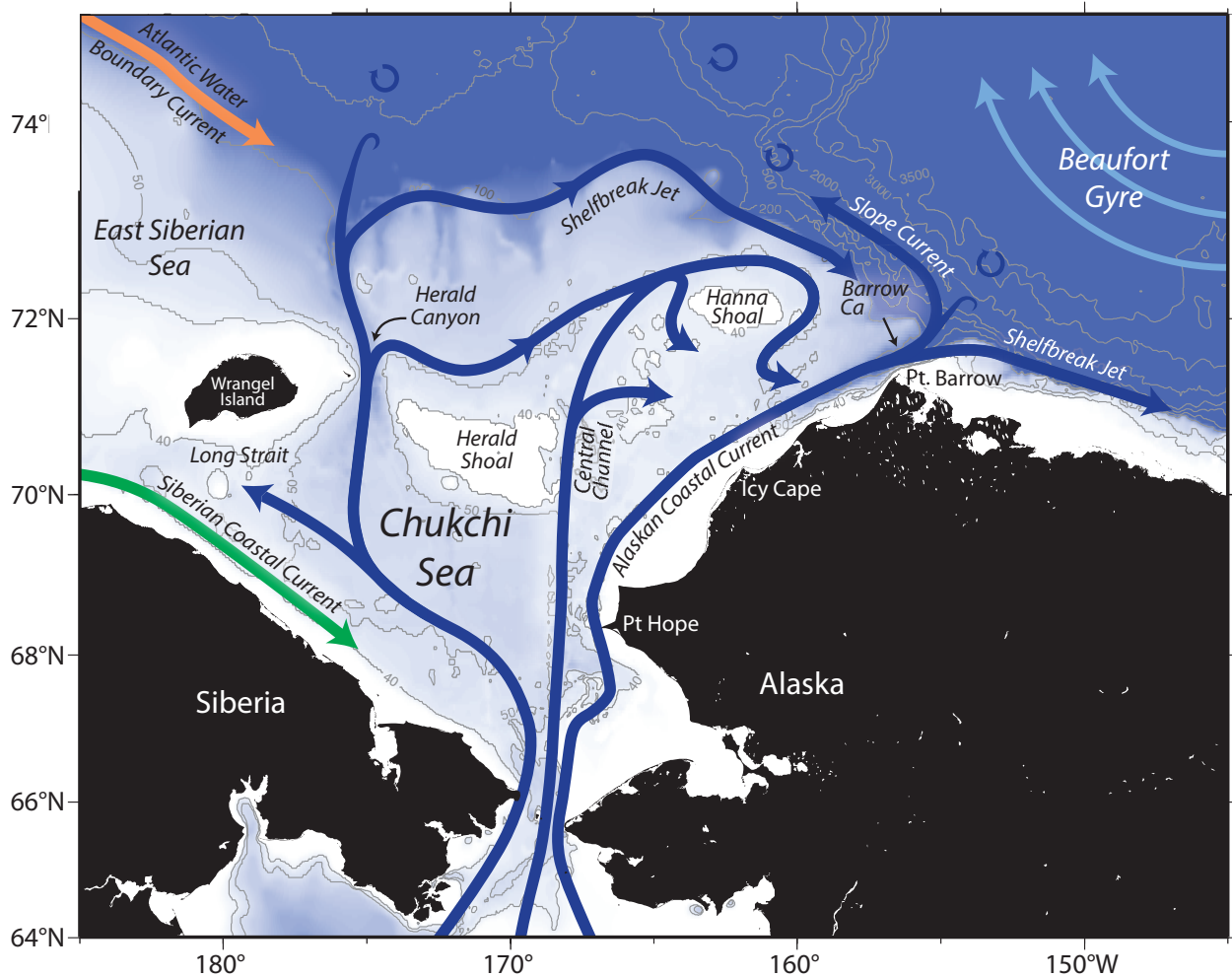
73
74   Figure 1. Circulation schematic of the Chukchi Sea and place names (from Corlett and Pickart,
75   2017). The bathymetry is from ETOPO2.
76

77   Barrow Canyon is an important choke point of the Chukchi circulation that influences the

78   export into the western Arctic. Roughly half of the annual Bering Strait inflow of Pacific Water

79   drains through the canyon (Itoh et al., 2013). It is thus important to understand the factors

80   controlling the circulation and its variability there. For example, what conditions determine

81   which water masses get upwelled through Barrow Canyon? What portion of the Chukchi shelf is

82   influenced by these upwelling events? Pisareva et al. (2019) found that upwelling sometimes

83   delivers denser water to the head of Barrow Canyon and other times delivers lighter water. They

84   noted that much of the difference was due to strong seasonality of the water masses present on

85   the Chukchi Shelf, i.e. the initial water mass. Unlike the findings of Lin et al. (2019b) for the

86   Alaskan Beaufort Slope, Pisareva et al. (2019) found that upwelling of Atlantic Water to the

87   head of Barrow Canyon occurs only infrequently. However, Itoh et al., (2013) report that AW is

88   maintained below ~150 m at the mouth of Barrow Canyon year round.

89   While strong northeasterly wind can force a flow reversal (upwelling) in Barrow Canyon,

90   flow is down-canyon under all other wind directions (Lin et al., 2019a). A sea surface height

91   gradient (pressure head) between the Pacific and Arctic Oceans is the primary driver of

92   northward flow through Bering Strait (Coachman & Aagaard, 1966; Woodgate et al., 2005b).

93   The signal of northward flow is largely coherent across the eastern Chukchi Sea (Woodgate et

94   al., 2005b). However, the northward flow is opposed by the mean wind in the region, i.e.

95   northeasterly wind along the northwest coast of Alaska (Pisareva et al., 2019) and northerly wind

96   in Bering Strait (Woodgate et al., 2005b). Woodgate (2018) found that the northward transport

97   through Bering Strait has been increasing in recent years and attributes that trend to an increase

98   in the pressure head. Danielson et al. (2014) propose that the increase in sea surface height on the

99   Bering Sea end of the Strait is due to an eastward shift in the mean position of the Aleutian Low.

100   Danielson et al. (2014) also present evidence of northward propagating shelf waves, which

101   follow the Alaska coastline, and can increase or decrease Bering Strait transport on synoptic time

102   scales, with the sign of the velocity signal depending on the direction of wind that sets up the

103   shelf wave. If flow through Bering Strait and across the Chukchi Sea is primarily driven by the

104   pressure head, but strongly modulated by local winds, do local winds near Bering Strait and near

105   Barrow Canyon always act in concert? What sort of dynamical response might there be if/when

106   they do not?

107   Although there has only been a slight warming in Bering Strait inflow waters, because of

the increased volume transport there has been a significant increase in heat transport through the strait (Woodgate, 2018). Serreze et al. (2016) found heat transport through Bering Strait to be the strongest predictor in timing of both spring ice retreat and fall ice advance. This additional heat flux can also promote sea ice thinning across much of the western Arctic Ocean (Woodgate et al., 2015). How apparent is the effect of seasonal variations in Bering Strait inflow on the spatial pattern of sea ice?

Polynyas are a common occurrence in the Arctic. As stated previously, northeasterly winds in the region of Barrow Canyon drive offshore Ekman transport that results in upwelling. Similar wind conditions can also drive offshore ice transport along the northwest coast of Alaska. Such regions of ice divergence along a coastline are known as wind-driven, or latent heat, coastal polynyas (Morales Maqueda, 2004). Because the water column in a wind-driven polynya remains at the freezing temperature, new ice is readily formed at the surface. Continued offshore transport of ice makes this type of polynya an ice production zone and contributes to the densification of the water column. Alternatively, sensible heat polynyas are formed when warm ocean waters are introduced to an ice-covered region, melting the existing ice and preventing new ice from forming. The location, extent, and duration of such polynyas are dependent upon the same characteristics of the warm water mass (Morales Maqueda, 2004). Hirano et al. (2016, 2018) provide evidence that the recurring polynya in the vicinity of Barrow Canyon is a hybrid latent and sensible heat polynya, influenced by both wind-driven ice divergence and upwelling of warm waters through Barrow Canyon. However, their analysis shows the influence of sensible heat on the polynya is limited to localized areas very near the coastline. Other investigators (e.g. Ladd et al., 2016) have suggested a much larger extent of warm water influence.

In this study we use data from an extensive set of moorings deployed across the Chukchi Sea in 2013-14, from Bering Strait to the western Beaufort Sea, to address some of the above questions. This allows us to explore the coupled nature of the flow across the shelf in relation to the wind forcing and the sea ice concentration. We begin with a description of the data sources utilized and the method used for identifying wind events in Section 2. In Section 3, we give a brief description of the mean flow over the study year. In Section 4, we explore the flow and water mass response in Barrow Canyon to northeasterly wind events. Section 5 investigates spatial patterns in sea ice on regional and local scales and their relationships with potential forcing mechanisms. Shelf-wide circulation patterns and their relationship to regional wind

Table 1. Mooring descriptions

ID	Lat (°N)	Lon (°W)	Water Depth (m)	Deployment Dates (mm/dd/yyyy)	ADCP Range (m)	Sample Int. (h)	Vertical Res. (m)	MicroCAT/ SeaCAT Depth (m)	Sample Int. (h)	Institution[a]
A2[b,c]	65°47	168°34	54	07/06/2013-07/01/2014	1-39	0.5	2	50	1	UW/APL
				07/03/2014-07/04/2015				50	1	
				07/03/2014-08/07/2014	1-39	0.5	2			
				08/07/2014-07/04/2015	1-37	1	4			
A3[b]	66°20	168°57	56	07/05/2013-07/02/2014	1-39	0.5	2	45	1	UW/APL
				07/02/2014-07/03/2015	1-39	0.5	2	43	1	
A4[b]	65°45	168°16	47	07/06/2013-07/01/2014	1-33	0.5	2	40	1	UW/APL
				07/03/2014-07/03/2015	1-33	0.5	2	40	1	
BCE	71°40	155°0'	107	09/06/2013-09/11/2014	3-75	2	4	93	1	JAMSTEC
BCH	71°19	157°9'	60	07/24/2013-07/23/2014	-	-	-	56	1	JAMSTEC
BCW	71°48	157°21	171	09/07/2013-09/11/2014	2-138	2	4	81	1	JAMSTEC
BC2	70°55	159°56	52	09/11/2013-09/23/2014	3-46	0.5	1	51	0.25	UAF
BS3	71°24	152°3'	147	10/21/2013-07/17/2014	10-115	1	5	40	12	WHOI
Bu	71°14	163°17	46	08/01/2013-08/05/2014	17, 35	0.25	-	38	0.25	ASL
Cj	71°10	166°45	47	07/31/2013-07/31/2014	21, 35	0.25	-	40	0.25	ASL
C1	70°50	163°7'	44	08/27/2013-09/25/2014	4-28	1	4	40	1	PMEL
C2	71°13	164°17	43	08/27/2013-09/26/2014	7-37	1	2	39	1	PMEL
C5	71°12	158°0'	53	08/31/2013-09/29/2014	5-33	1	4	44	1	PMEL
C6	71°47	161°52	42	08/28/2013-10/04/2014	13-39	1	2	39	1	PMEL
C7	72°25	161°36	42	08/29/2013-10/02/2014	4-32	1	2	41	1	PMEL
CS2	72°18	157°44	102	10/12/2013-09/22/2014	16-81	1	5	90	.25	WHOI
CS3	72°20	157°27	163	10/13/2013-09/22/2014	22-132	1	10	41	6	WHOI
CS4	72°23	157°9'	249	10/13/2013-09/22/2014	22-222	1	10	54	6	WHOI
CS5	72°26	156°50	357	10/13/2013-09/22/2014	31-331	1	10	44	6	WHOI
CT	72°13	166°58	48	10/09/2013-07/10/2014	8-38	1	5	46	0.25	WHOI
FM1	72°16	158°2'	67	10/25/2013-09/21/2014	13-53	1	5	61	0.25	UAF
NE40	72°7'	160°30	41	09/09/2013-09/18/2014	3-37	0.5	1	37	0.25	UAF
NE50	72°10	159°7'	50	09/09/2013-09/18/2014	4-46	0.5	1	46	0.25	UAF
NE60	72°11'	158°33	57	09/09/2013-09/18/2014	5-53	0.5	1	53	0.25	UAF
NW40	72°17	163°32	41	09/10/2013-09/20/2014	3-37	0.5	1	38	0.25	UAF
NW50	72°32	164°6'	51	09/09/2013-06/16/2014	4-47	0.5	1	47	0.25	UAF
SCH	68°2'	168°50	61	07/20/2013-07/19/2014	-	-	-	53	1	JAMSTEC

[a] University of Washington Applied Physics Laboratory (UW/APL), Japan Agency for Marine-Earth Science and Technology (JAMSTEC), University of Alaska Fairbanks (UAF), ASL Environmental Sciences, Inc. (ASL), National Oceanic and Atmospheric Administration Pacific Marine Environmental Laboratory (PMEL), Woods Hole Oceanographic Institution (WHOI)

[b] Two deployment years were spliced together in order to cover the entire study year, resulting in a small gap at turnaround. ADCPs contained significant errors in the surface bins, so those levels were omitted from the analysis (above 8 m at A2 and above 7 m at A3 and A4).

[c] While the MicroCAT operated without incident during the 2014 deployment, the ADCP experienced an error about one month in, which caused it to reset to factory defaults. Portion with 4 m vertical resolution was interpolated to 2 m resolution.

139

140 patterns are explored in Section 6. A summary of our results is presented in Section 7.

2. Data and methods

2.1. Moorings

In 2013, there was an extraordinary number of moorings deployed in the northeastern Chukchi Sea as a result of projects conducted by multiple institutions. Here we use data from 27
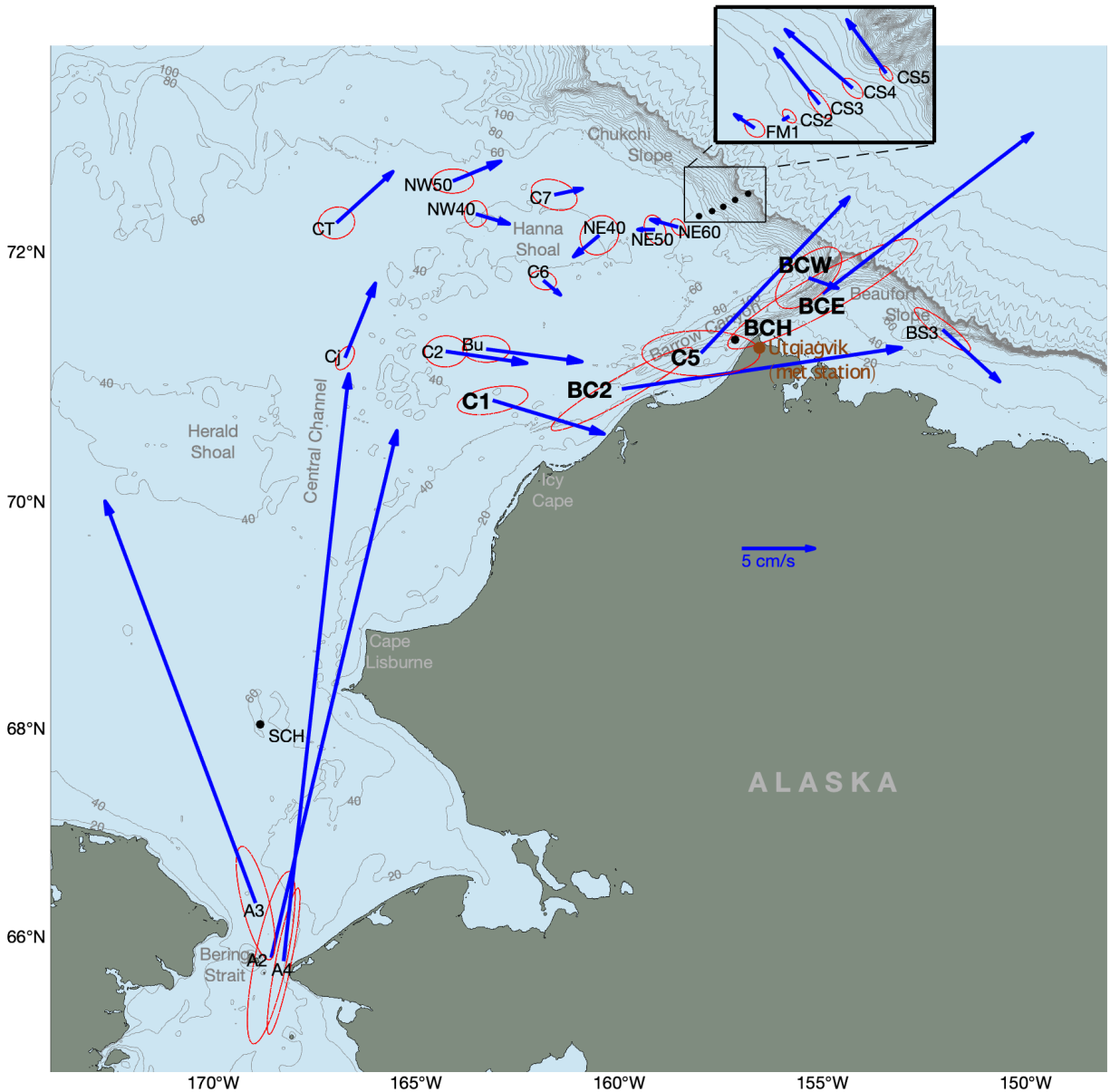
Figure 2. Mean depth-averaged velocity vectors for the study year (Oct 2013 – Sep 2014) with standard error ellipses. Bold lettering indicates moorings within the coastal pathway. Bathymetry contours at 20 m intervals to 500 m, then 500 m intervals. Note that no velocity data were collected at moorings BCH and SCH. The location of the meteorological station in Utqiaġvik is marked in brown.

151 moorings: 22 from the northeastern Chukchi shelf and adjacent slope, one from the Beaufort

152 slope, one from the southern Chukchi shelf, and three from Bering Strait (Table 1; Fig. 2).

153 Although the exact dates of deployment varied by project, seasonal access to the region limits

154 deployment and retrieval of moorings to summer/early-fall, which resulted in fairly consistent

155 coverage at all mooring sites.

156   For our analysis, we consider only data during the 12-month period from Oct 2013

157 through Sep 2014, which provides the most complete data coverage (Fig. 3). This choice of dates

158 restricts missing data at most moorings to a few weeks or less at the beginning and/or end of the

159 year. A few moorings have a longer gap. CT had a total deployment period of 9 months, with

160 most of the gap occurring at the end of our year. Cj, Bu, BS3, BCH, and SCH were retrieved in

161 late July/early August. The acoustic Doppler current profiler (ADCP) at NW50 and the

162 MicroCAT at CS5 both failed in mid-June. For the Bering Strait moorings, A2, A3, and A4, we

163 spliced together two separate deployments so there is a small gap at each mooring turnaround.

164   All of the moorings were equipped with SeaBird MicroCATs (SBE 37) or SeaCATs

165 (SBE 16 or SBE 19) measuring temperature, conductivity, and pressure near the bottom. With

166 the exceptions of SCH and BCH, all moorings were equipped with bottom-mounted, upward-

167 facing Teledyne RDI 300 or 600 kHz ADCPs. The velocity timeseries were de-tided using the

168 T_TIDE harmonic analysis toolbox (Pawlowicz et al., 2002), although the tides are much weaker

169 than the signals of interest. The largest tidal amplitudes observed were ~4 cm s^{-1}, although most

170 were ~1-2 cm s^{-1}. Mooring Cj had the largest tidal amplitude relative to variability in the full

171 velocity record. Here, the M2 tide had an amplitude of 3.5 m s^{-1} while the standard deviation in

172 velocity was 7.2 m s^{-1}. The rest of the moorings had lower tidal amplitudes and/or higher

173 standard deviations in velocity. Gaps in the timeseries were filled in using two-dimensional

174 Laplacian-spline interpolation. The vast majority of these gaps consisted of a few hours and/or

175 covered less than 10% of the measured water column. The most extensive set of gaps occurred at

176 C6 where there was a 30-day period in the mid-winter when readings throughout the top 1/3 of

177 the water column were intermittent. However, given the strongly barotropic nature of the flow,

178 these could reasonably be interpolated.

179   Sample intervals varied by mooring (Table 1). All mooring data were interpolated and/or

180 subsampled, as appropriate, to obtain hourly data. For all analyses of water velocity, the depth-

181 averaged flow (over the depth-range covered by the respective ADCP) is used. Across the study

182   region, the flow is largely barotropic. Because most mooring locations exhibit little variation of

183   flow speed and direction with depth, even though there is some inconsistency in the proportion

184   of the water column covered by each ADCP, the depth-averaged velocities are considered

185   representative of the full water column. Exceptions to that occur east of Hanna Shoal (NE40,

186   NE50, and NE60), across the Chukchi Slope (CS2-5), and on the Beaufort Slope (BS3). East of

187   Hanna Shoal, the surface layer is baroclinic and flow direction can vary greatly between surface

188   and bottom layers. Along the Chukchi and Beaufort Slopes, shelfbreak jets and the Chukchi

189   Slope Current generally manifest as a core of flow in the opposite direction of the waters above

190   or below them. For these locations, the depth-averaged velocity is still used to illustrate that

191   variability at these locations coincides with that of the large-scale flow patterns over the rest of

192   the study region (as discussed in section 6), but the reader should be aware that the vertical

193   structure is not represented. For discussions of vertical structure at these locations, the reader is

194   referred to Fang et al. (2020) and Tian et al. (2021) for the area east of Hanna Shoal, Li et al.,

195   (2019) for the Chukchi Slope, and Nikolopoulos et al. (2009) for the Beaufort Slope.

196   *2.2. Wind conditions*

197   For broad-scale wind conditions, we used the 10-m winds from the ERA5 reanalysis

198   (Hersbach, 2018) from the European Center for Medium-Range Weather Forecasts (ECMWF,

199   https://www.ecmwf.int/). ERA5 is the fifth-generation product, an updated version of ERA-

200   Interim, with higher spatial and temporal resolutions of 0.25° and 1 hr, respectively. Here we use

201   3-hourly resolution.

202   To identify wind events that potentially drive upwelling in Barrow Canyon, we use the

203   wind record from the meteorological station at Utqiaġvik, AK (formerly Barrow, AK). The

204   hourly wind data for the study period were obtained from the National Climate Data Center of

205   the National Oceanic and Atmospheric Administration (http://www.ncdc.noaa.gov/). The data

206   have been subsequently quality controlled by removing outliers and interpolating over small gaps

207   (see Pickart et al., 2013, for details) , and are widely used in studies of the northern Chukchi Sea

208   and western Alaskan Beaufort Sea (e.g., Lin et al., 2016; Lin et al., 2019b). For the full record

209   (1941-2017), the mean wind speed was 2.06 m s^{-1} directed along 257°T. For the dates of the

210   study year the mean wind speed was 1.64 m s^{-1} along 256°T. Using 230°T as the positive along-

211   coast direction in the vicinity of Barrow Canyon, a minimum wind speed threshold was chosen

212   which best captured discrete wind events (i.e., time periods when northeasterly wind was visibly
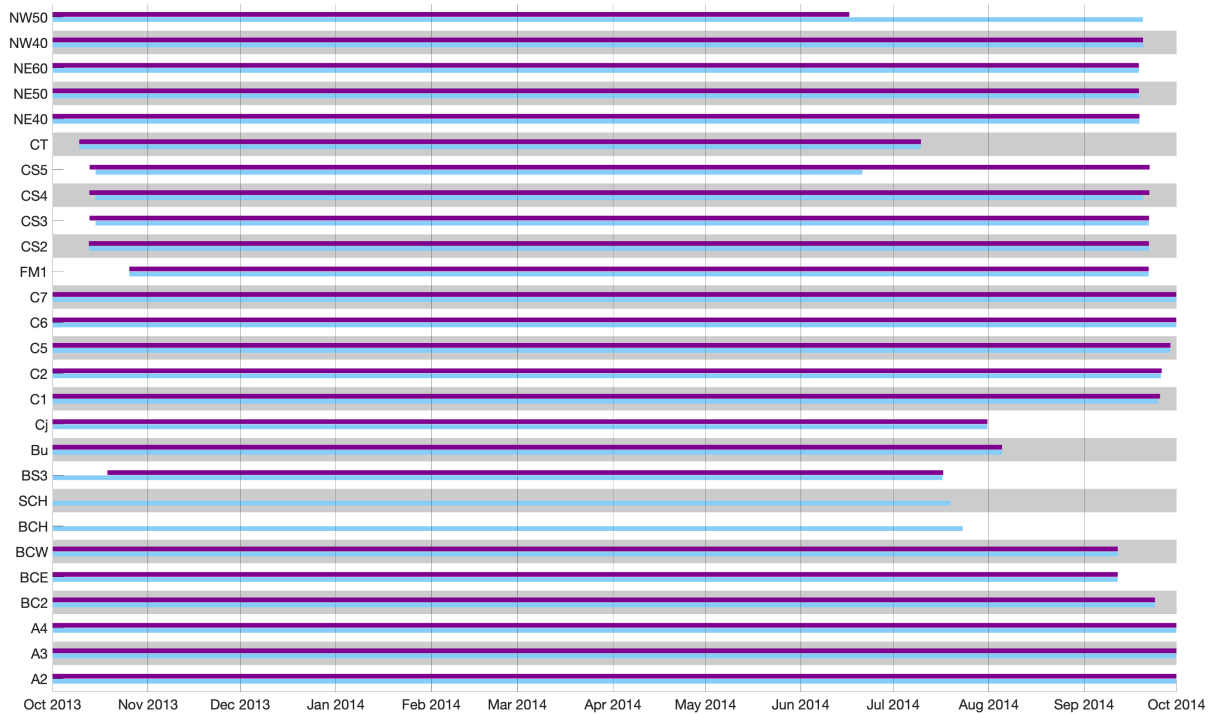
Figure 3. Data coverage at each mooring over the study year, defined as 1 Oct 2013 – 30 Sep 2014. Purple lines indicate dates for velocity data and blue lines indicate dates for temperature/salinity/pressure data.

stronger than background levels). We identified events as having an along-coast wind speed greater than 4 m s^{-1} sustained for at least 24 hours. Once the 24-hour minimum is met, a reduction of along-coast wind speed for up to 12 hours is permitted within the event. Thus, the beginning of an event is the first hour that along-coast wind speed exceeds 4 m s^{-1}, the duration is the time period during which all criteria are met, and the end of the event is the last hour that wind speed exceeds 4 m s^{-1} (after which there is more than 12 hours of reduced wind speeds).

Using these criteria, we identified 23 wind events over the course of the year (Table 2). However, these thresholds allow for significant variability in wind direction. Lin et al., (2019a) found that flow reversals in Barrow Canyon only occur under northeasterly winds, but a strong east-southeasterly wind can still have an along-coast component above 4 m s^{-1}. For the purposes of evaluating the water column response to northeasterly wind events, we use the six events with the clearest signal of sustained northeasterly wind. These were events with a clear beginning and end, which maintained a northeasterly wind direction throughout. The purpose of being selective in these events was to get a clear picture of the water column response to northeasterly winds in the absence of other influencing factors. Wind events identified by local winds are labeled E1-

233 Table 2. Wind event details. Stars indicate the clear northeasterly events used for the upwelling
234 response analysis. Shading indicates events occurring during the full-ice period.
235

Designation	Start (2013)	End (2014)	Duration (hrs)	Mean Wind Speed (m s^{-1})	Max Wind Speed (m s^{-1})
E1	8 Oct	10 Oct	45	7.9	14.9
E2	13 Oct	14 Oct	27	7.5	10.1
E3*	19 Oct	21 Oct	42	7.6	10.6
E4*	22 Nov	25 Nov	66	7.6	12.5
E5	5 Dec	7 Dec	45	7.8	10.1
E6	8 Dec	10 Dec	42	7.4	12.2
E7*	21 Dec	22 Dec	33	7.8	10.6
E8	27 Dec	9 Jan	306	7.7	15.0
E9	17 Jan	29 Jan	280	7.8	14.2
E10*	14 Feb	18 Feb	99	5.9	8.9
E11	22 Feb	24 Feb	43	7.2	9.2
E12	26 Feb	28 Feb	53	7.3	11.2
E13*	11 Mar	12 Mar	26	6.2	7.9
E14	13 Mar	15 Mar	54	5.6	8.6
E15	18 Apr	23 Apr	103	5.0	8.8
E16	27 Apr	29 Apr	51	7.8	10.9
E17*	27 May	2 Jun	147	8.7	12.7
E18	8 Jun	12 Jun	89	5.0	7.4
E19	18 Jun	23 Jun	109	6.8	9.7
E20	26 Jun	28 Jun	56	5.7	6.9
E21	7 Jul	11 Jul	92	6.4	8.9
E22	7 Aug	17 Aug	253	8.7	14.7
E23	9 Sep	21 Sep	294	6.8	10.7

236 E23 (Table 2). The six clear northeasterly events are E3, E4, E7, E10, E13, and E17 (designated

237 with an asterisk in Table 2).

238 *2.3. Ice concentration*

239   The daily ice concentration data used in this study are provided by the Remote Sensing of

240 Sea Ice Research Group at the University of Bremen (https://seaice.uni-bremen.de/). The data are

241 obtained by applying the ARTIST (Arctic Radiation and Turbulence Interaction STudy) Sea Ice

242 algorithm (Spreen et al., 2008) to the original measurements of the new Advanced Microwave

243 Scanning Radiometer (AMSR2) launched in 2012 (Beitsch et al., 2014), as the successor of

244 AMSR-E. The resolution of the product is 3.125 km in our study region.

245 **3. Mean shelf-wide flow**

246   The depth-averaged mean flow for the study year shows many of the features observed in

247 previous studies (Fig. 2; see also Tian et al. (2021) who analyzed the same set of moorings).

248   There is strong inflow through Bering Strait (A2-A4, mean 29.5-40.6 cm s^{-1}), and evidence of

249   the two pathways on the eastern side of the Chukchi Sea. The coastal pathway (bold-lettered

250   mooring locations) corresponds to high velocities as water drains from the shelf via Barrow

251   Canyon (mean at BC2 is 19.4 cm s^{-1}). The relatively low mean velocity at BCW (2.1 cm s^{-1}) is

252   due to the fact that flow out of the canyon at this location ranges from northwestward to

253   southeastward and much of this variability cancels out in the mean. The Central Channel

254   pathway bifurcates in the vicinity of Cj (mean 5.5 cm s^{-1}): one branch flows eastward (C2 and

255   Bu) towards Barrow Canyon, and the other branch continues northward towards CT before being

256   diverted eastward around the north side of Hanna Shoal (means near Hanna Shoal range from

257   1.2-3.6 cm s^{-1}). The mean southeastward flow at C6 is consistent with either cyclonic flow

258   around the south side of Hanna Shoal or a retroflection towards Barrow Canyon after

259   anticyclonic flow around the north side of Hanna Shoal. The eastward flowing Beaufort

260   Shelfbreak Jet is seen at BS3 (mean 5.3 cm s^{-1}), and the westward flowing Chukchi Slope

261   Current is evident at CS3-5 (mean 5.3-7.0 cm s^{-1}). There is a hint of the eastward-flowing

262   Chukchi Shelfbreak Jet at CS2; however, the jet is bottom intensified with oppositely directed

263   flow in the surface layer, resulting in a depth-averaged mean flow close to zero (Li et al., 2019).

264   **4. Upwelling response in Barrow Canyon**

265   *4.1. Composite water column response*

266   The duration of the six northeasterly wind events (see section 2.2 for details on selection

267   criteria), varied from 26 hours to 147 hours, with mean along-coast wind speeds of 5.9 – 8.7 m s[-]

268   [1]. By normalizing time, with $t = 0$ and $t = 1$ corresponding to the first and last hours that wind

269   speed thresholds were met (refer to section 2.2), we created a composite timeseries of wind

270   speed for the six events (Fig. 4a). We then created corresponding composites of the depth-

271   averaged velocity (Fig 4b-f) at the five mooring sites along the coastal pathway that had ADCPs

272   (four in Barrow Canyon and one upstream). The moorings along the coastal pathway are labeled

273   with bold lettering in Fig 2, including mooring BCH which has no velocity data. The composites

274   show a strong reversal of direction from the mean flow that occurs nearly simultaneously with

275   the change in wind speed. For most of the moorings in Barrow Canyon, the reversed flow is up-

276   canyon along the canyon axis. The flow at C5 appears anomalous, but is in fact in the up-canyon

277   direction along the local bathymetry at that site. The flow response at C1 on the shelf, ~100 km

278   upstream of the canyon, illustrates the tightly coupled nature of upstream flow and the flow in
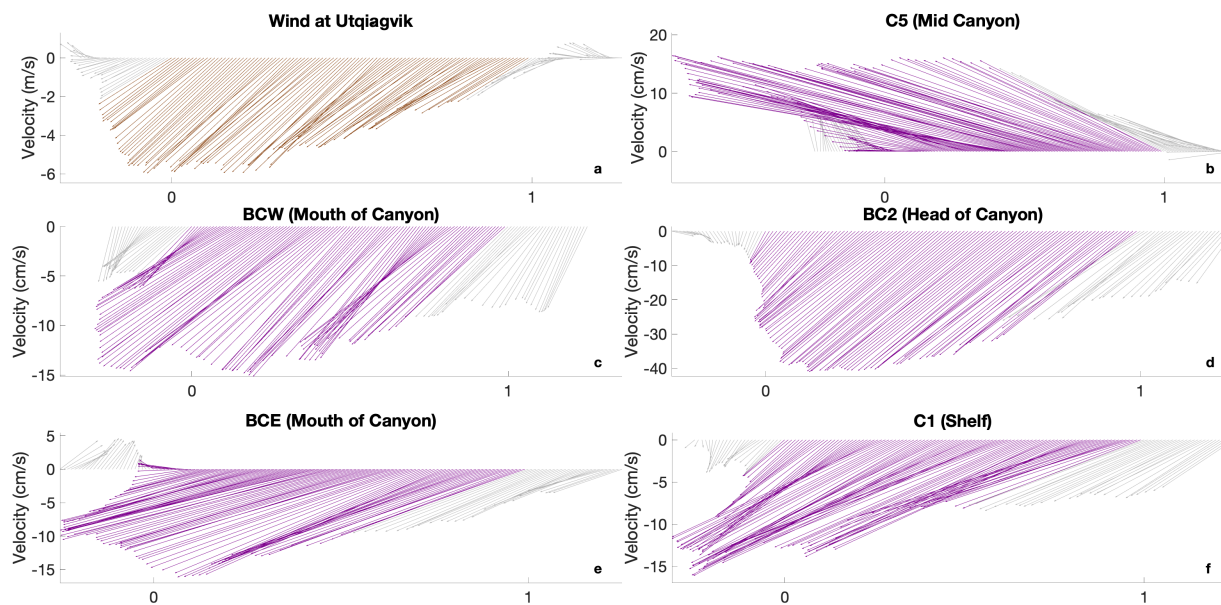
Figure 4. Composites constructed using normalized time (see text for details). Colored vectors represent velocities over the wind event duration. Gray vectors represent velocities preceding and following the event, each over a duration of 25% of the event length. (a) Wind velocity at Utqiaġvik met station. (b-f) Depth-averaged velocity at moorings in and upstream of Barrow Canyon.

Barrow Canyon. Over the entire year, the principal component of velocity (i.e., the component along the axis of maximum variance) at C1 and BC2 (at the head of the canyon) are highly correlated (r = .87). As seen in the composites, the water column response at C1 occurs just as quickly as at BC2.

The strong reversal of flow seen in the composites at each mooring site is representative of the water column response during individual wind events. The pre-event composite (gray vectors preceding $t = 0$) is included to illustrate the distinct change in flow that occurs with the onset of northeasterly winds. However, pre-event conditions are highly variable, ranging from strong down-canyon (or other non-reversed direction) flow, to weak flow, to strong flow in the reversed direction. The pre-event portion of the composites should not be taken as representative of background conditions. The composites at all five mooring sites show a lag in the relaxation of flow after the end of the event (gray vectors following $t = 1$). However, this is not true for all of the individual events.

4.2. Velocity response to wind event strength

Next, we assess the relationship between the strength of a wind event and the strength of the depth-averaged flow response. To quantify the strength of a wind event, we calculated the

14

302   cumulative Ekman transport over the duration of each event:

303
$$CET = \int_{t_s}^{t_e} \frac{\tau_a(t)}{f\rho_0} dt,$$

304   Where τ_a is the along-coast component of the wind stress (following Large and Pond, 1981), ρ_0

305   is a representative water density for the region, f is the Coriolis parameter, t_s and t_e correspond

306   to the start and end times of the event (as described in section 2.2). Thus, cumulative Ekman

307   transport takes into account both the magnitude and the duration of the event.

308   Similarly, the strength of the flow response was calculated as a cumulative velocity

309   anomaly from the initial condition:

310
$$CVA = \frac{1}{H} \int_{t_s}^{t_e} \int_{bot}^{top} (v(z,t) - v_0(z)) \, dz \, dt$$

311   where v_0 is the velocity at the beginning of the event, v is the velocity at each time step, and H is

312   the total depth over which the velocity is measured. Since several of the mooring sites do not

313   exhibit rectilinear flow (i.e., $\sim180°$ offset between reversed and non-reversed directions),

314   velocity here is simply categorized as negative when in the general direction of the mean flow

315   and positive when in a direction that would collectively lead to a reversed flow path, and the full

316   magnitude of velocity is used. This allows for a comparison of flow reversal for mooring sites

317   with a variable non-reversed flow direction. This categorization of flow is also beneficial at C1,

318   where the mean flow is largely eastward, but the reversed flow often has a significant southward

319   component. Calculating the response as an anomaly from the initial condition allows for events

320   that start with strong down-canyon flow to be compared with events that start when there is

321   already up-canyon flow. Calculating CVA as a depth-averaged velocity allows for comparison of

322   sites with different depths.

323   Using CET to quantify wind event strength and CVA to quantify water column response,

324   we find that, overall, stronger events induce a stronger response (Fig. 5, where the wind event

325   strength is plotted on a log scale). It must be kept in mind, however, that this is based on the six

326   events with the clearest signal of sustained northeasterly winds. When considering all 23 events

327   (not shown), the pattern is less clear. While there is still a general increase in response strength

328   with increasing wind event strength, there is significantly more scatter about this trend.

329   There is also an apparent difference in velocity response by mooring site. One would
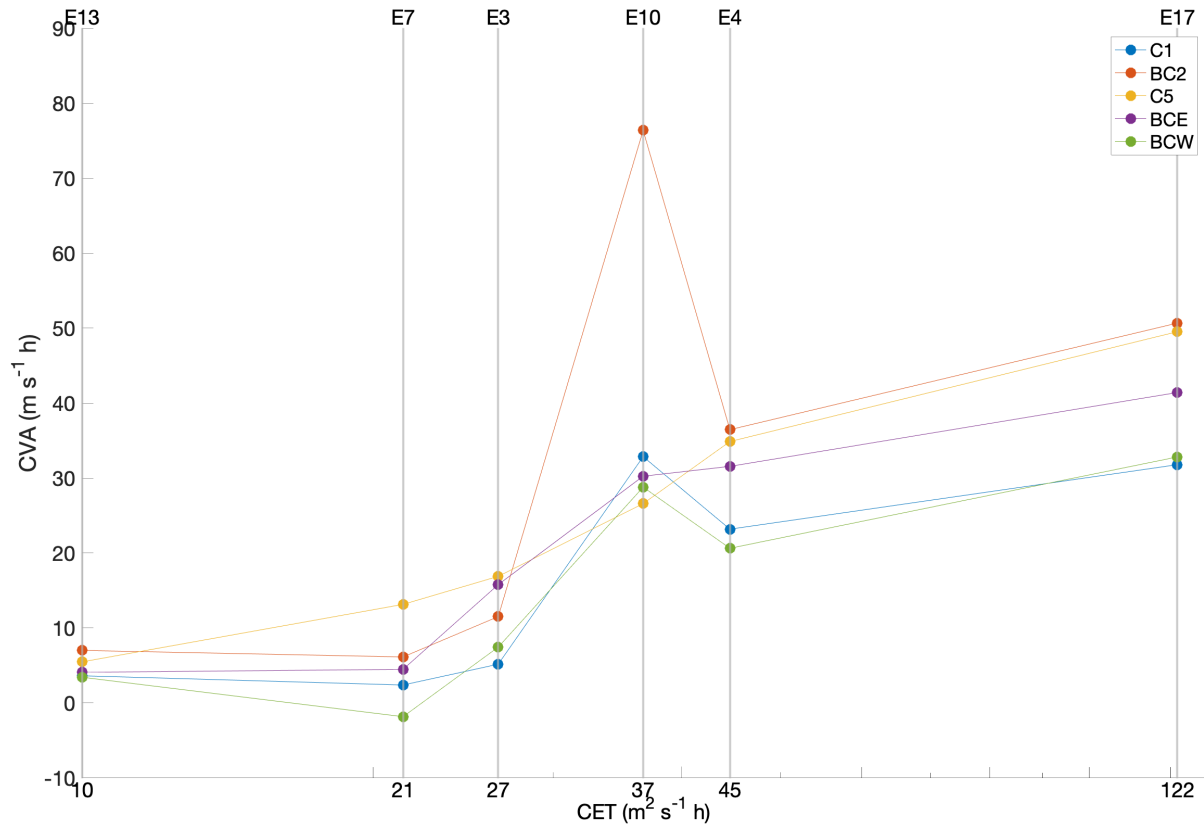
Figure 5. Comparison of wind event strength (CET) to velocity response (CVA) at each mooring along the coastal pathway. CET is plotted on a log scale.

expect an Ekman-related response to diminish with distance from the coast. Indeed the moorings farthest from the coast (BCW and C1) consistently have the lowest response strength (except for E10). However, the geometry of the canyon and a simple conservation of mass argument may also provide sufficient explanation. BCW and C1 have the deepest and widest channels, respectively, allowing the response to be distributed over a larger area. BC2 and C5 generally have the highest response strength. Both of these moorings are located where the canyon narrows (in a reversed-flow perspective), which would concentrate the response. E10 has an anomalously large response at BC2, C1, and BCW. At these sites, strong up-canyon flow continues for more than two days after the winds have subsided at Utqiaġvik, with BC2 being the last site to resume down-canyon flow. The delay for upwelling to relax as the winds decrease could explain the anomalous response at these locations.

During the course of the year, some of the upwelling events begin prior to the onset of northeasterly winds at Utqiaġvik (one upwelling event begins a full week prior), some of the events continue after winds subside, and two weak upwelling events occur in the absence of

16

348   northeasterly winds. This and the scatter in the relationship between event strength and velocity

349   response suggests the influence of other forcing, perhaps related to propagating shelf waves.

350   Using an idealized numerical model, Danielson et al. (2014) show that winds over the Bering

351   Sea can initiate shelf waves that propagate northward along the Alaska coastline and can induce

352   a velocity response in both Bering Strait and Barrow Canyon. In a generalized linear model

353   exploring the relationship between reanalysis wind fields and a mooring array at the head of

354   Barrow Canyon (which included mooring site BC2 from the current study, although during an

355   earlier year), Danielson et al. (2014) find that remote winds account for a significant proportion

356   of the transport. We do see potential indicators for a role of propagating shelf waves in our

357   analysis, although it is not a dominant effect. This is being addressed in an ongoing study.

358   *4.3. Water mass response to upwelling*

359   As mentioned earlier, much of the water that flows across the Chukchi Sea eventually drains

360   through Barrow Canyon. There is significant interannual variability in water mass properties, but

361   we adopt a generalized classification of water masses based on potential temperature and salinity

362   ranges used in previous studies (e.g., Pickart et al., 2019; Pisareva et al., 2019). In the spring and

363   summer, the inflow through Bering Strait is relatively warm and fresh. The two Pacific-origin

364   summer water masses are Bering Summer Water [BSW] and Alaskan Coastal Water [ACW],

365   with ACW being warmest and freshest (Table 3). During the cold months of the year, Newly

366   Ventilated Winter Water [NVWW] is advected through Bering Strait. This water mass is close to

367   the freezing point and can be further transformed locally on the Chukchi shelf via convective

368   overturning in polynyas and leads (Weingartner et al., 1998; Pickart et al., 2016; Pacini et al.,

369   2019). NVWW eventually warms to become Remnant Winter Water [RWW] due to solar

370   heating and/or mixing with summer waters (e.g. Gong & Pickart, 2016). RWW constitutes the

371   cold halocline of the interior western Arctic (Woodgate, 2012), where it is more generally

372   referred to as Pacific Winter Water. Finally, cold and very fresh water is classified as Melt

373   Water [MW], which can also include river runoff.

374   Due to a variety of factors, including differences in the transit times for each of the flow

375   paths and the melt/freeze cycle of the pack ice, the seasonality of water masses in Barrow

376   Canyon is not the same as in Bering Strait (e.g. Tian et al., 2021). For example, NVWW can be

377   found in the canyon in late-summer, having arrived via the central pathway and around Hanna

378   Shoal (Fang et al., 2020; Pickart et al., 2019). Barrow Canyon also sees intermittent appearances

379   Table 3. Water mass definitions

Water Mass	Abbreviation	Salinity Range	Potential Temperature Range (ºC)
Melt Water	MW	0 – 30	any
		30 – 31.5	< 0
Alaska Coastal Water	ACW	30 – 32	> 3
Bering Summer Water	BSW	30 – 33.6	0 – 3
		32 – 33.6	> 3
Newly Ventilated Winter Water	NVWW	> 31.5	< -1.6
Remnant Winter Water	RWW	31.5 – 33.6	-1.6 – 0
		> 33.6	-1.6 – -1.26
Atlantic Water	AW	> 33.6	> -1.26

380

381   of Atlantic Water [AW] associated with upwelling events. Bear in mind, however, that the

382   hydrographic sensors on the moorings are situated near the bottom and therefore will not detect

383   lighter summer waters if they are confined to the surface layer.

384   While there was a clear relationship between wind event strength and velocity response,

385   there is no apparent connection between event strength and the properties of the upwelled water.

386   Our measurements reveal that some upwelling events result in a density increase at the head of

387   Barrow Canyon and others result in a density decrease, as observed by Pisareva et al. (2019), but

388   we also find that many upwelling events are associated with little density change. Overall, the

389   relative density change is largely dependent on the water mass present at the head of the canyon

390   at the start of an event, which is seasonally varying. For example, at the start of E3 there is light

391   BSW at the head of the canyon (Fig. 6a). This relatively weak wind event (refer to Fig. 5) results

392   in the upwelling of RWW to BC2. The much stronger E17 starts with NVWW at the head of the

393   canyon and brings only more NVWW to BC2 (Fig. 6b). The final water mass has a lower density

394   than the initial water mass. The density of the final water mass for both events is near 26.0 kg m^{-}

395   ^{3} and the magnitude of the density change is larger for the weaker event.

396   The absence of a direct link between wind events and water properties in Barrow Canyon

397   motivates us to explore the water mass signatures over the entire year (Fig. 7). Because of the

398   multiple moorings available, we can get a sense of the progression of water masses along the

399   length of the canyon. Pickart et al. (2019) found that upwelling water masses bank up against the

400   eastern flank of Barrow Canyon, which could be related to the higher velocity responses we
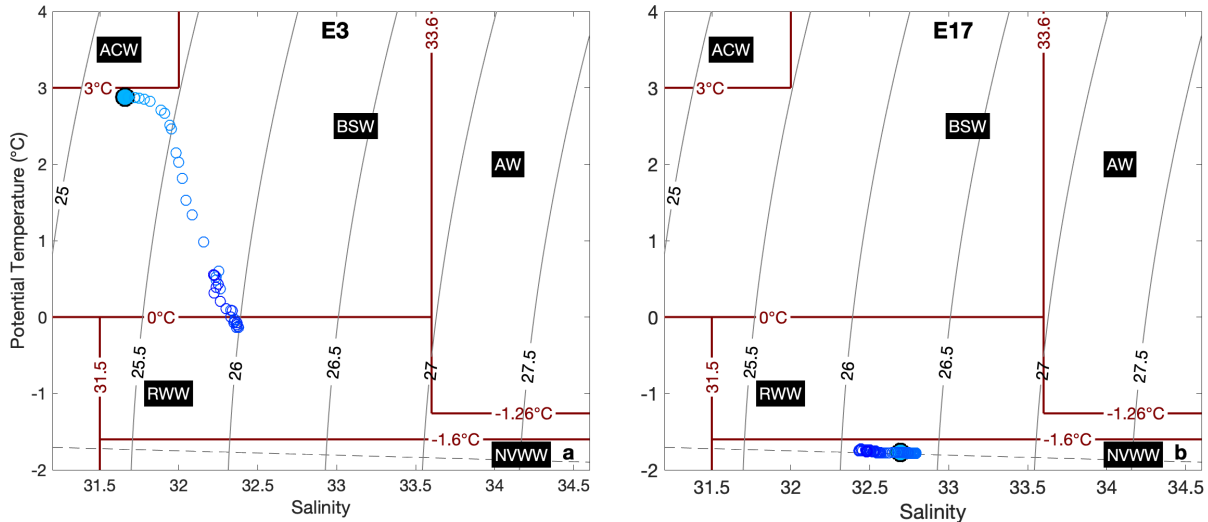
Figure 6. Water properties at mooring BC2 over the course of wind events (a) E3 and (b) E17. The large filled circles indicate the initial water properties. Smaller unfilled circles represent the properties at each time step, darkness of color indicates passage of time. Dark red lines delineate water mass boundaries as defined in Table 3.

found at BCE, C5, and BC2. We also find that water masses present at BCW (on the western side of the canyon mouth) have little relationship to the water masses present at the other moorings along the canyon. For this reason, we focus on the mooring sites on the eastern side of Barrow Canyon. The most obvious feature is a strong seasonality, which matches well with that described by previous studies except that summer waters were late to arrive in 2014 (although they may have been present earlier at shallower depths). Summer waters are present from Oct-Nov 2013 and return Sep 2014, while NVWW occupies the canyon from Dec through mid-Jul. With the exception of brief appearances at BCE and BCH, AW is not measured at all in summer and is only present episodically in late fall and winter. During each of these episodes, AW progresses from the mouth of the canyon towards the head and coincides with reversed flow at the head of Barrow Canyon (black bars at top of Fig. 7). Each time the AW is preceded by RWW (recall that cold halocline water in the interior of the Arctic Basin also fits within this definition). AW only reaches C1, upstream of Barrow Canyon, during one upwelling event (late Jan). Because AW was only detected for a total of 13 hours, it simply appears as a dark line in the figure. With four years of data, Ladd et al. (2016) recorded 5 upwelling events which resulted in AW at C1, so it is indeed uncommon. It is worth noting that, in many cases, upwelled water masses reach BCH before BCE (note blocks of AW in Fig. 7). The reason for this is unclear, but
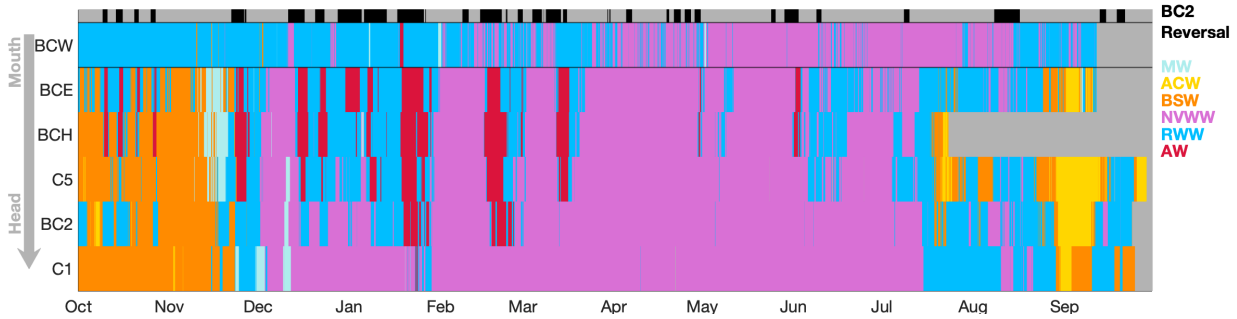
Figure 7. Timeseries of water masses present along Barrow Canyon and just upstream at C1 (coastal pathway). Water mass abbreviations are defined in Table 3. Black bars at the top indicate times when the flow is up-canyon at BC2.

may simply reflect that the water mass shoals along the length of the canyon more readily than at the mouth of the canyon. The combination of flow over shoaling bathymetry and through a narrowing channel would cause the lifting of isopycnals along the canyon to outpace their lifting at the mouth.

Comparing water masses to the direction of flow at the head of Barrow Canyon (BC2, see Fig. 7) allows us to identify patterns associated with upwelling events regardless of whether or not they are associated with northeasterly wind at Utqiaġvik. We see that AW only reaches the head of Barrow Canyon (BC2) in the winter, after a series of long upwelling events. From mid-December through the beginning of February, there isn't sufficient time between upwelling events for the RWW to drain completely from the canyon. Over the first half of February, NVWW once again flushes out the canyon. The next long upwelling event, in mid-February, results in a swift return of AW to the canyon, suggesting that water from the previous upwelling event may not have fully receded into the basin. Nikolopoulos et al. (2009) found that the interface between Pacific winter water and AW in the Arctic Basin is higher in the water column in late-fall and winter, which could also affect the availability of AW for upwelling into Barrow Canyon.

5. Patterns in ice cover

5.1. Seasonality of regional ice cover

To assess the relationship between ice cover and the circulation across the eastern Chukchi shelf, we first performed an empirical orthogonal function (EOF) analysis of the regional ice cover extending from 174°W to 147°W and 65°N to 74°N (roughly the domain of Fig. 2). The year-long mean ice concentration for 2013-14 is shown in Fig. 8a. As one would expect, there is an overall gradient associated with higher mean ice concentrations in the north

20

452 and lower mean ice concentrations in the south. Also visible in the mean is a signature of the

453 three main inflow pathways across the Chukchi Sea. These appear as tongues of lower mean

454 concentration along the northwest coast of Alaska, extending northward in Central Channel, and

455 extending northwestward towards Herald Canyon (out of the domain). There are also isolated

456 patches of low mean ice concentration adjacent to the northwest coast of Alaska, which reflect

457 the occurrence of polynyas.

458   We first provide a brief overview of the two primary modes, followed by more detailed

459 discussion of each. Mode 1 (Fig. 8b,d), which explains 73% of the variance, depicts the entire

460 domain varying with the same sign as it transitions from the negative state to the positive state in

461 fall and then back to the negative state in spring. By contrast, mode 2 (Fig. 8c), which accounts

462 for 12% of the variance, depicts the northern and southern portions of the domain varying with

463 opposite signs. The mode 2 amplitude timeseries (Fig. 8e) reveals that this mode has background

464 conditions in the positive state and enters the negative state during the same time periods that

465 mode 1 transitions between states. These fall and spring time periods correspond to the periods

466 of freeze-up and melt-back seen in the full record. We, therefore, conclude that mode 1

467 represents the transition between summer and winter conditions and mode 2 represents the
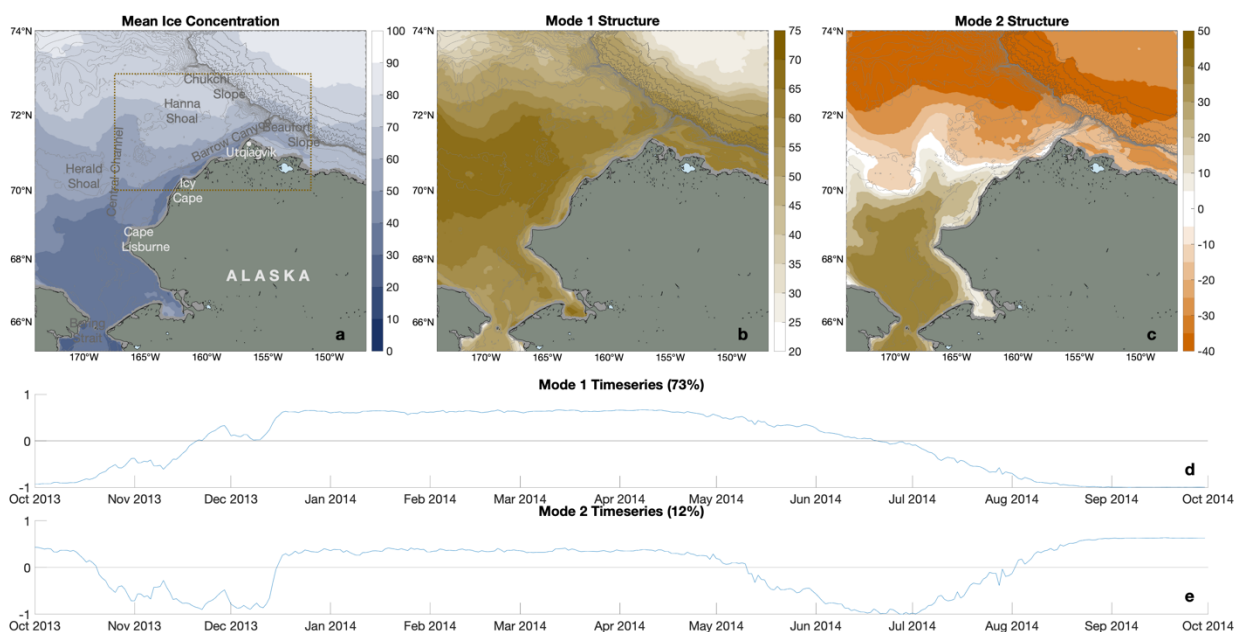
468
469 Figure 8. Large-scale EOF of ice cover over the study year. (a) Mean ice concentration. (b)
470 Structure function for mode 1. (c) Structure function for mode 2. (d) Modal amplitude timeseries
471 for mode 1. (e) Modal amplitude timeseries for mode 2. The box in (a) delimits the smaller
472 spatial domain represented in the local ice EOF below.

473 pattern of variability during the fall freeze-up and spring melt-back periods.

474 *5.1.1. Mode 1: Summer and winter states*

475   Over the course of the year, ice cover ranges from completely open water across the

476 domain in summer to completely ice covered, with concentrations near 100%, across the domain

477 in winter. The modal amplitude timeseries for mode 1 (Fig. 8d) illustrates this transition, with the

478 maximum negative state describing summer conditions and the maximum positive state

479 describing winter conditions. The structure of this mode (Fig. 8b) shows the entire domain

480 varying with the same sign. All points are above their mean in winter and below their mean in

481 summer. The middle of the domain (roughly 69°N to 72°N) shows the greatest variance, while

482 the northern region (ice covered much of the year) and southern region (open water much of the

483 year) show less. There is little evidence of the inflow pathways in the structure of this mode.

484 *5.1.2. Mode 2: Freeze-up and melt-back*

485   The mode 2 structure (Fig. 8c) is oppositely signed in the northern and southern regions

486 of the domain. The positive state has the effect of making the ice concentration across the

487 domain more uniform, while the negative state has the opposite effect, increasing the north-south

488 concentration gradient. Notably, the mode 2 structure shows the signature of the inflow

489 pathways. When added to the mean, the structure function diminishes this signature during

490 summer and winter, and enhances it during freeze-up and melt-back (not shown). Similar

491 magnitudes of the mode 2 timeseries during freeze-up and melt-back show that the pattern is

492 equally evident in both time periods. The ability of these pathways to enhance melt-back in

493 spring is commonly noted (e.g., Spall, 2007; Woodgate et al., 2010), while our analysis

494 highlights the fact that these pathways can also act to delay freeze-up in the fall.

495   Both modes portray melt-back as a smooth transition occurring over approximately three

496 months. The mode 1 timeseries shows melt-back as a linear transition from full ice to open

497 water. The mode 2 timeseries shows it as a transition from uniform conditions to a strong north-

498 south concentration gradient and back to uniform conditions. With the exception of 20-23 May,

499 there is consistent northward flow through Bering Strait over this time period and the inflow

500 pathways are apparent in the mode 2 pattern of melt-back. The freeze-up process is less smooth,

501 but only takes about two months. Mode 1 shows it as occurring in several steps. Mode 2 shows it

502 as a sharp transition from uniform conditions to a strong gradient, temporarily backtracking

503 twice, and then a sudden jump back to uniform conditions. The two periods where the freeze-up

504 stalls are associated with stronger northward flow through Bering Strait. The signature of the

505 three inflow pathways is particularly evident at these times.

506   It is notable that, although evidence of polynyas exists in the mean concentration field,

507 there is no clear mode that describes the occurrence of polynyas. Instead, the signature of the

508 polynyas emerges in layers of increasing detail over many modes. An analysis over the full

509 length of the AMSR2 record (2012-2020, not shown) reveals that the seasonal pattern is highly

510 consistent. Spatial patterns of the mean and first two modes are nearly identical to those shown

511 for the 2013-14 study year. Freeze-up always takes ~2 months, while melt-back lasts 3-4

512 months. Melt-back is usually a smooth process, while freeze-up is often marked by interruptions.

513
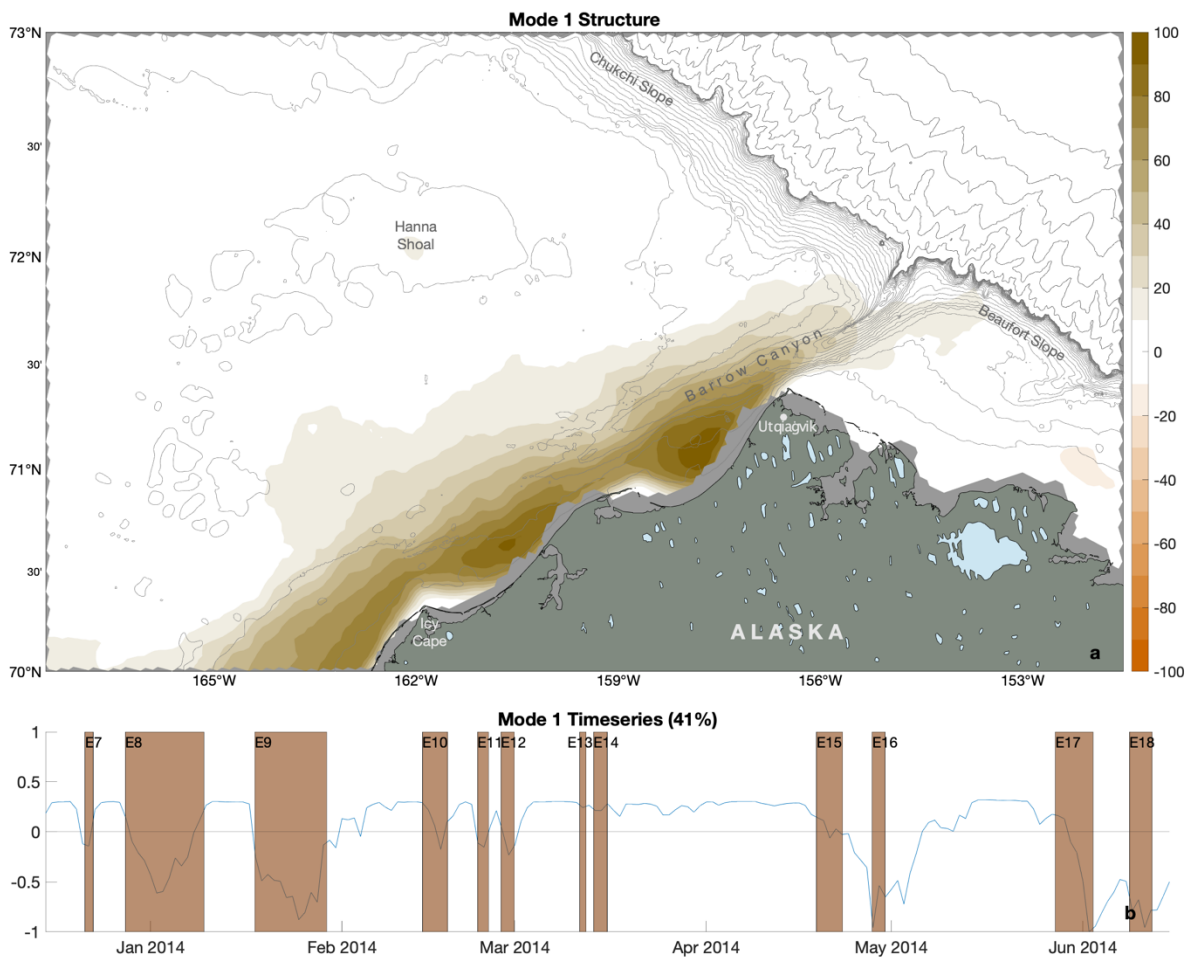
514
515 Figure 9. Mode 1 of the local EOF of ice concentration over the full-ice period (15 Dec – 15
516 Jun). (a) Structure function. (b) Modal amplitude timeseries, where the shading indicates
517 duration of northeasterly wind events identified at Utqiaġvik during this time period.
518

519 *5.2. Interconnectedness of local ice cover, wind forcing, and upwelling*

520   The large-scale pattern of ice cover is dominated by the seasonal signal. To explore more

521 localized features and their relationship to both wind and upwelling events, we also performed an

522 EOF analysis of ice cover with a more limited spatial and temporal domain. Here, we consider

523 ice concentration extending from 167.5°W to 151.5°W and 70°N to 73°N (corresponding to the

524 box outlined in Fig. 8a), which contains all mooring sites except those in the southern Chukchi

525 Sea and Bering Strait. Limiting the analysis to 15 Dec 2013 – 15 Jun 2014 (the season of nearly

526 full ice cover for this spatial domain) eliminates the seasonal signal entirely and provides a look

527 at the pattern of polynya formation.

528 *5.2.1. Local ice EOF mode 1*

529   Mode 1 (Fig. 9) for this more limited space/time domain accounts for 41% of the

530 variance in the record. The structure shows regions of reduced ice cover adjacent to the coastline,

531 consistent with the expected pattern of wind-driven coastal polynyas. The modal amplitude
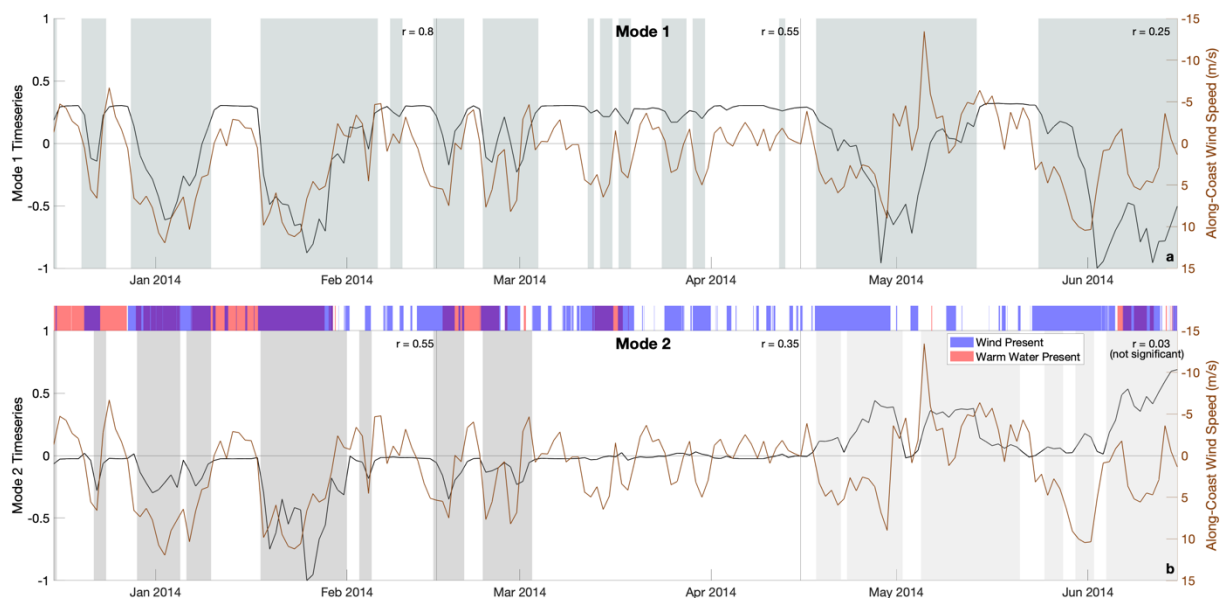

532
533 Figure 10. Comparison of the local ice concentration EOF to potential forcing sources. (a) Mode
534 1 timeseries (black) and along-coast wind at Utqiaġvik (brown, inverted). Gray shading indicates
535 negative excursions of the mode. (b) Mode 2 timeseries (black), along-coast wind at Utqiaġvik
536 (brown, inverted). The dark gray shading indicates the negative excursions of the mode during
537 the winter period. The light gray shading indicates the positive excursions of the mode during the
538 spring period. The colors along the top depict when warm water was present at mooring C5 (red)
539 and when positive along-coast wind occurred (blue). Overlapping of these two conditions results
540 in purple segments. Correlation coefficients are noted for each two-month period in both (a) and
541 (b), see text for details.

542

24

543   timeseries (Fig. 9b) shows a background condition in the positive state with intermittent

544   excursions into the negative state, where the negative state corresponds to a reduction in ice

545   concentration in the region of the polynyas. The background condition resides in the positive

546   state due to a similar spatial pattern of slightly reduced ice concentration that shows up in the

547   mean (not shown). Negative peaks match up well with the northeasterly wind events (Fig. 9b).

548   We note that only four of the six events selected earlier for the upwelling analysis fall within the

549   full-ice period, so we now consider all 12 events identified during this time (Table 3).

550   The mode 1 timeseries is positively correlated (r = 0.46) with the daily mean along-coast

551   wind speed. Closer inspection, though, reveals that the correlation starts out much higher and

552   diminishes over the season (Fig 10a). From mid-Dec to mid-Feb, a period dominated by two

553   strong wind events and large polynyas, the mode 1 timeseries is highly correlated with the wind

554   (r = 0.80). From mid-Feb to mid-April, a period of weaker winds and much lower polynya

555   response, the correlation is still good (r = 0.55). With the ice likely at its thickest and most

556   tightly-packed state, a lower wind response is not surprising. From mid-April to mid-Jun, the

557   correlation is low (r = 0.25, although still significant at the 95% confidence level). Strong along-

558   coast winds are still associated with large a polynya response, but the polynyas do not close back

559   up quickly when the wind dies down. At this time of year, the ice edge is approaching the

560   southern part of the domain, indicating that conditions are becoming unfavorable for ice

561   formation.
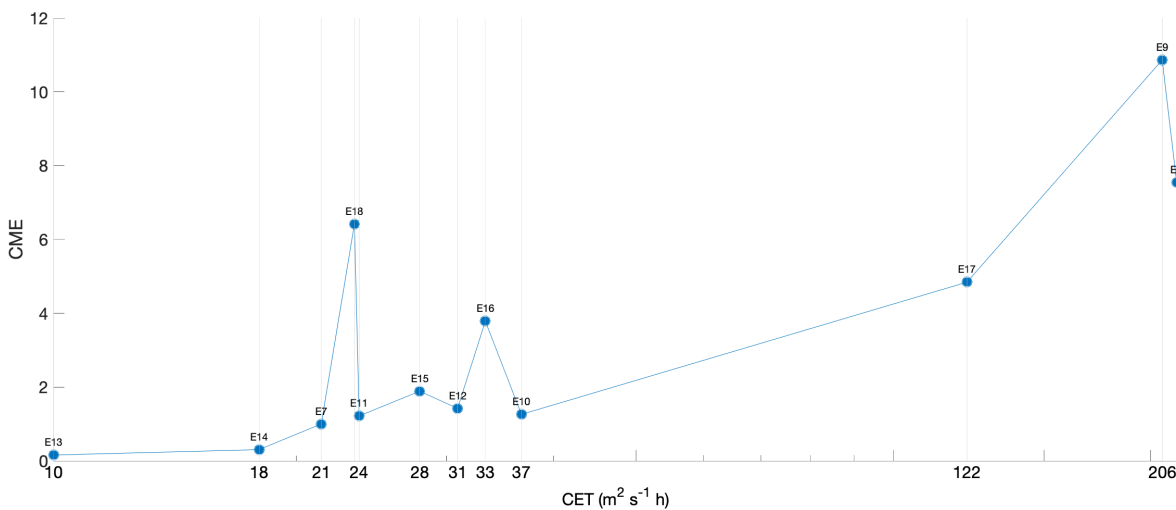
562
563   Figure 11. Comparison of wind event strength (CET) to the local ice EOF mode 1 response
564   (CME). CET is plotted on a log scale.
565
566

567 *5.2.2. Mode 1 response relative to wind event strength*

568   Recall that we characterized the strength of a wind event by the cumulative Ekman

569 transport, which takes into account both the magnitude of the wind stress and the duration of the

570 event. We now similarly quantify the polynya response as a cumulative modal excursion from

571 the background state over the duration of the event:

572
$$CME = -\int_{t_s}^{t_e} M(t) - M_0 \, dt$$

573 where $M(t)$ is the value of the modal amplitude at time t and M_0 is the value of the modal

574 amplitude in its background state. The sign is reversed simply to produce a positive value for

575 easier comparison with wind event strength. This reveals a clear linear relationship between the

576 event strength (recall that we are considering all 12 wind events identified during this time) and
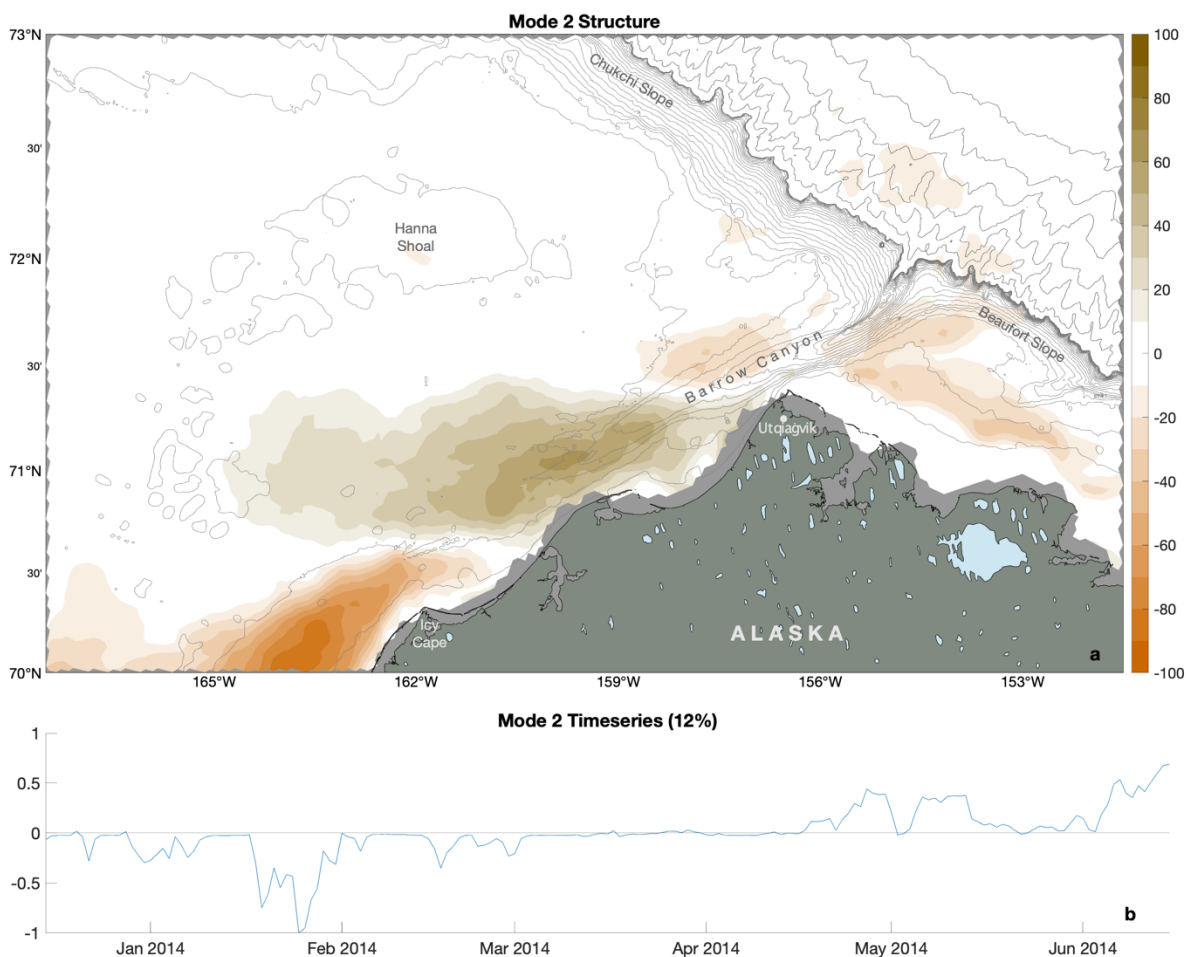
577
578 Figure 12. Mode 2 of the local EOF of ice concentration over the full-ice period (15 Dec – 15
579 Jun). (a) Structure function. (b) Modal amplitude timeseries.
580

581 the polynya response (Fig. 11). There are two major outliers to this relationship, E16 and E18.

582 Both of these events occur towards the end of the full-ice season and are the second in a pair of

583 events (Fig. 9b). As noted previously, at this time of year polynyas do not readily close when the

584 wind speed decreases. At the start of each of these events, a polynya is still open from the

585 previous event, enabling a much larger polynya to form than would otherwise be expected.

586 *5.2.3. Local ice EOF mode 2*

587 The orthogonal nature of EOF modes usually results in timeseries where a strong

588 response in one mode corresponds to a time of little to no response in other modes. However,

589 since polynyas tend towards being discrete events, the timing of the responses depicted in modes

590 1 and 2 of this EOF often coincide. However, the magnitude and/or sign of the response in each

591 mode are quite different (as is the spatial pattern). Mode 2 (Fig. 12) accounts for 12% of the

592 variance in the record. The structure shows a polynya response (a discrete area of decreased ice

593 concentrations in the negative state) that extends from the head of Barrow Canyon westward

594 across the shelf (centered near 71°N). The modal amplitude timeseries shows a background

595 condition at a neutral state with excursions into the negative state in the winter and excursions

596 into the positive state in the spring.

597 *5.2.4. Winter polynyas*

598 Since mode 2 shows some degree of response for nearly every polynya that mode 1 does,

599 mode 2 also shows some correlation to along-coast wind speed (Fig. 10b). While the correlation

600 between mode 2 and wind speed diminishes over the season just as it did with mode 1, the

601 correlation for each time period is much lower. In fact, in the final two months, there is no

602 significant correlation. Additionally, because the mode 2 polynya response is centered offshore

603 and extends obliquely rather than parallel to the coast, it is not consistent with a wind-driven

604 coastal polynya.

605 To explore the relationship between each of these modes and wind, we now take a closer

606 look at wind direction when each mode shows an opening polynya (i.e., ice concentration is

607 decreasing). As noted earlier, each mode exhibits a background state indicative of no polynya.

608 We then identify periods of polynyas opening up as times when the modal amplitude for each

609 mode exceeds a threshold below its background state and is lower than the previous day. If we

610 look at the wind at all times when mode 1 is in its background state, we see that wind speeds are

611 usually below 6 m s^{-1} and directions range from northwesterly to southwesterly (Fig. 13a), with

612
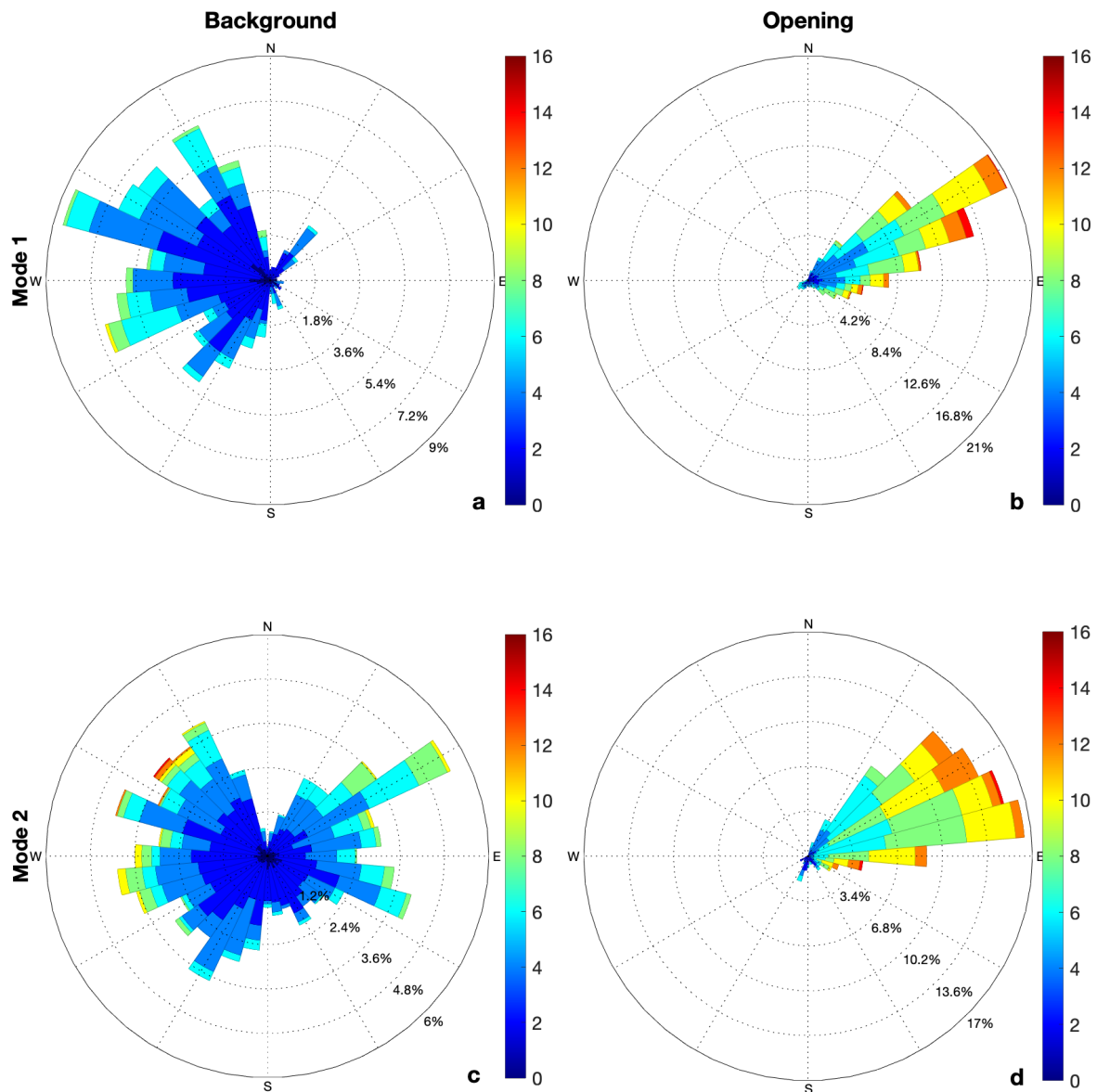
Figure 13. Wind roses showing wind speed (color, m/s) and direction for wind at Utqiaġvik under various conditions of the local ice concentration EOF. The first row pertains to mode 1 and the second row pertains to mode 2. (a,c) Wind under background conditions, i.e., when the respective mode depicts no polynya response. (b,d) Wind while each mode depicts a polynya opening up.

few exceptions. By contrast, when mode 1 shows a polynya opening up, wind speeds are

generally much higher, and the direction is almost exclusively northeasterly (Fig. 13b). Mode 2

shows a similar configuration of winds during opening of polynyas (Fig 13d). This is not

surprising, since both modes often show an opening polynya at the same time. However, during

624 times when mode 2 is in its background state, winds can be from any direction, including

625 northeasterly (Fig. 13c). This suggests that northeasterly winds are not the main factor inducing a

626 polynya response in mode 2.

627   The location and shape of the mode 2 response is consistent with a melt-driven polynya

628 associated with warm water being advected onto the shelf via Barrow Canyon. Temperature

629 records along Barrow Canyon indicate some correspondence between the presence of warmer

630 (above freezing) water and the mode 2 polynya response. The best relationship between water

631 temperatures and mode 2 polynyas is seen at C5, which frequently receives RWW and AW

632 during upwelling events and is also located near the leading edge of the mode 2 polynya. Yet,

633 mode 2 only shows a polynya response about half of the time that warm water is present at C5. It

634 is not until we put both the wind record and the temperature record at C5 together that a pattern

635 emerges (colored bars in Fig. 10b). The mode 2 polynya response roughly corresponds to times

636 when there is both a positive along-coast wind and warm water present at C5. The relationship is

637 not perfect, but it must be kept in mind that the mooring temperature sensors are situated near the

638 bottom and it is near-surface temperatures that would induce ice melt. Thus, we conclude that the

639 mode 2 response represents the influence of warm water on wind-driven polynyas and that it is

640 an indicator of upwelled warm water outcropping to the surface. More generally, reduced ice

641 cover in such a pattern offshore could be used to identify warm water upwelling events in the

642 absence of in situ measurements.

643   This assessment of both wind and warm water exerting influence on the recurring

644 polynya near Barrow Canyon is consistent with the assertion by Hirano et al. (2016, 2018) that

645 this is a hybrid latent and sensible heat polynya. The foundation of the argument that these

646 authors make is that purely wind-driven (latent heat) polynyas are areas of constant ice

647 production and so maintain frazil ice at their surface. These areas lose heat to the atmosphere as

648 new ice is formed. The introduction of warm water, on the other hand, prevents ice production

649 and creates areas of open water. In these areas, heat loss to the atmosphere is due to cooling of

650 surface water. So, while areas of sensible and latent heat influence cannot be differentiated

651 through atmospheric heat flux, areas of sensible heat influence can be identified by regions of

652 open water. They then estimate the influence of warm water on the polynya by calculating sea

653 ice production (based on atmospheric heat flux) with and without an open water mask. In both

654 illustrated cases in the 2016 study and in the long term mean in the 2018 study, the region

655   influenced by warm water masses based on identified areas of open water are quite localized and

656   very near the coastline. The spatial structure of our mode 2 suggests a very different pattern of

657   warm water influence. Ladd et al. (2016), based on four years of measurements at C1, also make

658   an argument for a larger spatial extent of upwelled warm water influence on sea ice. Hirano et al.

659   (2018) do show a single day in Jan. 2013 when the open water region extends farther offshore (to

660   approximately 163°W at 71°N).

661   The assumption that the sensible heat influenced portion of the polynya can be identified

662   by areas of open water seems to underestimate its spatial extent. The open water condition will

663   not be met if the heat input from upwelled water masses is insufficient to completely melt the ice

664   cover. This situation seems most likely in regions of ice convergence, such as would be expected

665   on the margins of a wind-driven polynya. Areas where upwelled warm water results in

666   incomplete melting of sea ice would not result in additional atmospheric heat flux, as all oceanic

667   heat flux goes into melting ice, and so does not impact estimates of sea ice production. If ice is

668   advected offshore and then melted in the area of upwelled water, this suggests a mechanism by

669   which sustained ice production in a coastal polynya can result in no increase of ice across the

670   shelf.

671   *5.2.5 Spring polynyas*

672   The reversal of sign in mode 2 in the spring indicates a regime change in polynya

673   response that is not seen in mode 1. Similar to the negative winter excursions, the positive spring

674   excursions of mode 2 occur intermittently within the mode 1 response (Fig. 10). Thus, they can

675   also be viewed as an enhancement of the mode 1 polynyas. Whereas the winter polynyas tended

676   to be focused around the head of Barrow Canyon, spring polynyas are focused at the southern

677   end of the domain with a reduced polynya signature near Barrow Canyon. This is consistent with

678   persistent NVWW in the canyon at this time (Fig. 7). The increased polynya activity at the

679   southern end of the domain occurs as the ice edge is approaching and may be associated with an

680   influx of warmer water through Bering Strait. Bottom temperatures at SCH (southern Chukchi

681   Sea) begin to increase above freezing in mid-May, but we don't have enough information to

682   draw a definitive conclusion there. While such a scenario would mark the transition of decreased

683   ice concentrations from being polynya-related to melt-back related, the frequency of polynyas in

684   this area mean that the two conditions often overlap. We note that, until the last week of the

685   analysis, there is a distinct region of ice off of Cape Lisburne which separates the polynya

686   formed/expanded during E17 from the ice edge and open water to the south.

687   *5.2.6. Limitations of this analysis*

688   The above analysis depicts a pattern of polynya formation that provides additional insight

689   into the sensible heat vs. latent heat (wind-driven) influences to what previous studies have

690   found. While we would prefer the two modes to cleanly describe the wind-driven and melt-

691   driven portions of polynya formation without conflating the effects of an approaching ice edge, it

692   is only through the combination of the southern enhancement due to the approaching ice edge

693   and the warm-upwelling effect that a strong enough signal emerges. This is an important

694   limitation of the results of this EOF analysis, and makes it sensitive to the choice of date range

695   evaluated. A similar analysis for the full length of the AMSR2 record (2012-2020, not shown)

696   exhibits similar spatial features. The first mode shows a polynya response parallel to the

697   coastline nearly identical to that of the study year. However, the spatial pattern shown in mode 2

698   in the study year appears to be split between modes 2 and 3 in the longer record. In the longer

699   record, mode 2 is a polynya response focused around the head of Barrow Canyon along with the

700   southern enhancement that shows up in spring polynyas, and mode 3 is a polynya response

701   centered offshore to the south of Barrow Canyon and extending westward. As such, the sum of

702   modes 2 and 3 is similar to mode 2 for our study year. This likely reflects the fact that warm

703   water is upwelled into Barrow Canyon more frequently than it is upwelled onto the shelf south of

704   the canyon.

705   **6. Shelf-wide response to wind forcing**

706   Thus far it has been shown that northeasterly wind events are responsible for flow

707   reversals in Barrow Canyon as well as the formation of polynyas along the coast. We now

708   investigate variations in flow patterns across the full study area and explore their relationship to

709   wind forcing. To do this, we performed an EOF analysis of hourly velocity (u and v) at all 25

710   moorings equipped with an ADCP (this excludes BCH in Barrow Canyon and SCH in the

711   southern Chukchi Sea).

712   *6.1. Velocity EOF mode 1*

713   Mode 1, which explains 49% of the variability in the record, describes a coherent change

714   in circulation across the entire domain. To compare the effect of the positive and negative states

715   of this mode, we have added the structure function at ± 1 standard deviation of the modal

716   amplitude to the mean velocities at each mooring (Fig. 14a-b). The positive 1 standard deviation
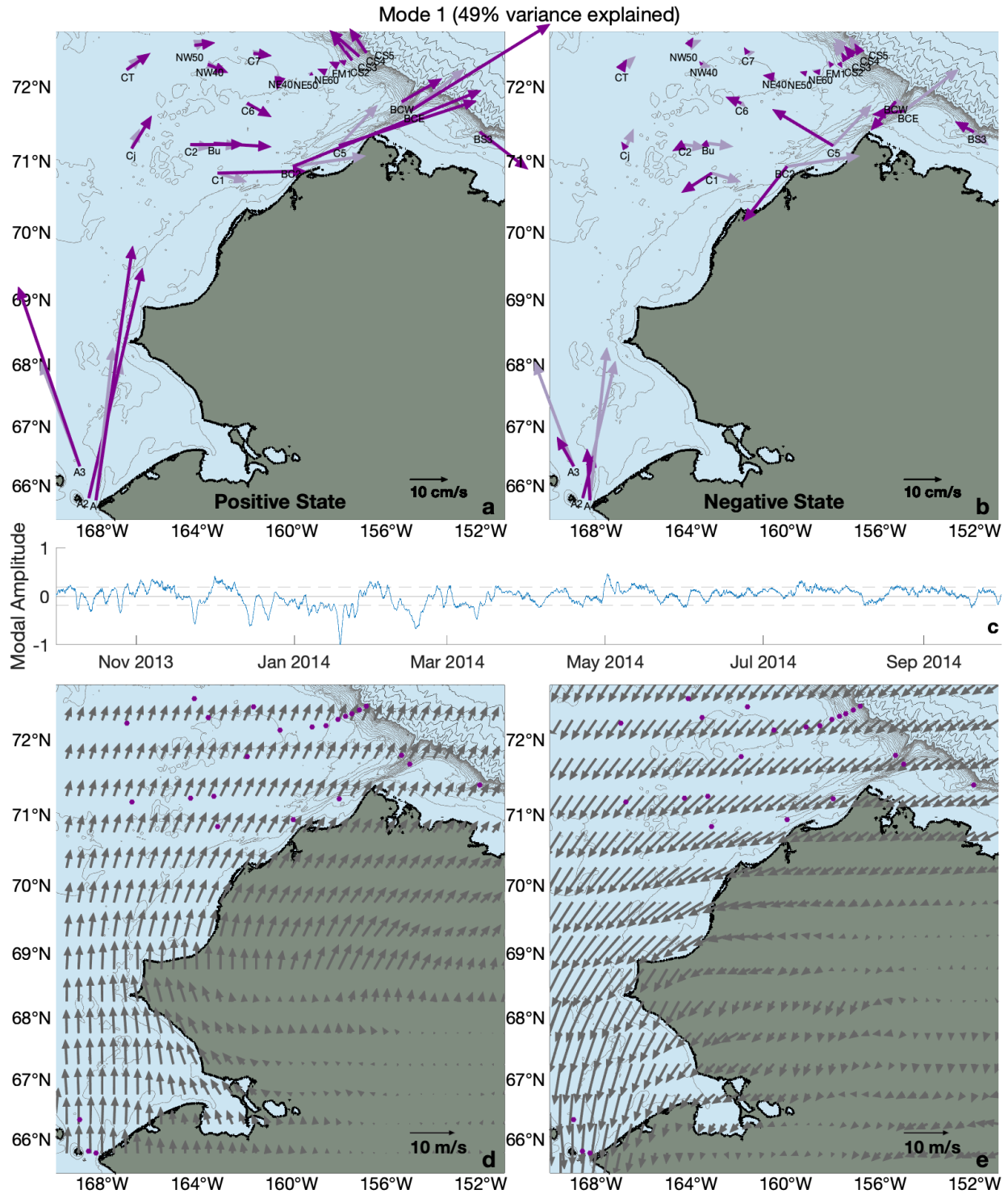
Figure 14. EOF mode 1 of mooring velocities (a) Mean velocities shown in light purple,
structure function at +1 standard deviation added onto mean shown in dark purple. (b) Same as
(a), but for -1 standard deviation. (c) Modal amplitude timeseries. (d) Composite ERA5 10 m
wind field for all times when EOF mode 1 is above +1 standard deviation. The mooring locations
are indicated by purple dots. (e) Same as (d), but for all times below -1 standard deviation.

724   state is largely an enhancement of the mean flow. Most moorings show a velocity around 2-3

725   times their mean, although the moorings just east of Hanna Shoal show little change. The

726   negative 1 standard deviation state shows a reversal of flow in Barrow Canyon, at all of the sites

727   south of Hanna Shoal and east of Central Channel (C1, C2, Bu, and C6), and at BS3 on the

728   Beaufort Slope. There is still northward flow in Bering Strait, although it is reduced to about one

729   third of the mean. Flow also slows across the northernmost parts of the shelf and the Chukchi

730   Slope.

731   Although the positive state exceeds one standard deviation many times over the course of

732   the year (Fig. 14c), it is usually only by a small amount. During the winter, the negative state

733   frequently exceeds one standard deviation, many times by a large amount. At these stronger

734   values of the negative state, flow reversal is seen at all of the mooring sites. This can result in

735   strong southward flow in Bering Strait (up to 2.5 times stronger than the magnitude of the mean

736   flow). East of Hanna Shoal and onto the upper Chukchi Slope, velocities remain small and the

737   term "reversed" is somewhat subjective since flow here is far from rectilinear. Extreme flow

738   reversals in Barrow Canyon and the nearby shelf can be close to ten times the magnitude of the

739   mean flow.

740   *6.2 Mode 1 relationship to regional wind*

741   To explore the connection of the positive and negative state mode 1 flow regimes to wind

742   forcing, we used the ERA5 10 m winds to create composite wind maps for all times when the

743   modal amplitude timeseries exceeded one standard deviation in each direction. When mode 1 is

744   higher than one standard deviation above the mean (11.5% of record), the wind field composite

745   (Fig. 14d) reveals a dominant southerly wind through Bering Strait, accounting for the enhanced

746   northward flow there. The composite also shows the dominance of southwesterly wind along the

747   northwest coastline of Alaska, enhancing the flow along the coastal pathway. Individual wind

748   fields during these times (not shown) reveal that the wind actually varies from southwesterly to

749   southeasterly. Mean winds along the northwest coastline of Alaska are northeasterly, so one

750   would expect to see flow stronger than the mean under any other wind direction (consistent with

751   the results of Lin et al., 2019).

752   When mode 1 is lower than one standard deviation below the mean (14.8% of record),

753   the wind field composite (Fig. 14e) reveals a dominant northerly wind through Bering Strait,

754   accounting for reduced northward flow there (which is reversed in stronger negative states). The
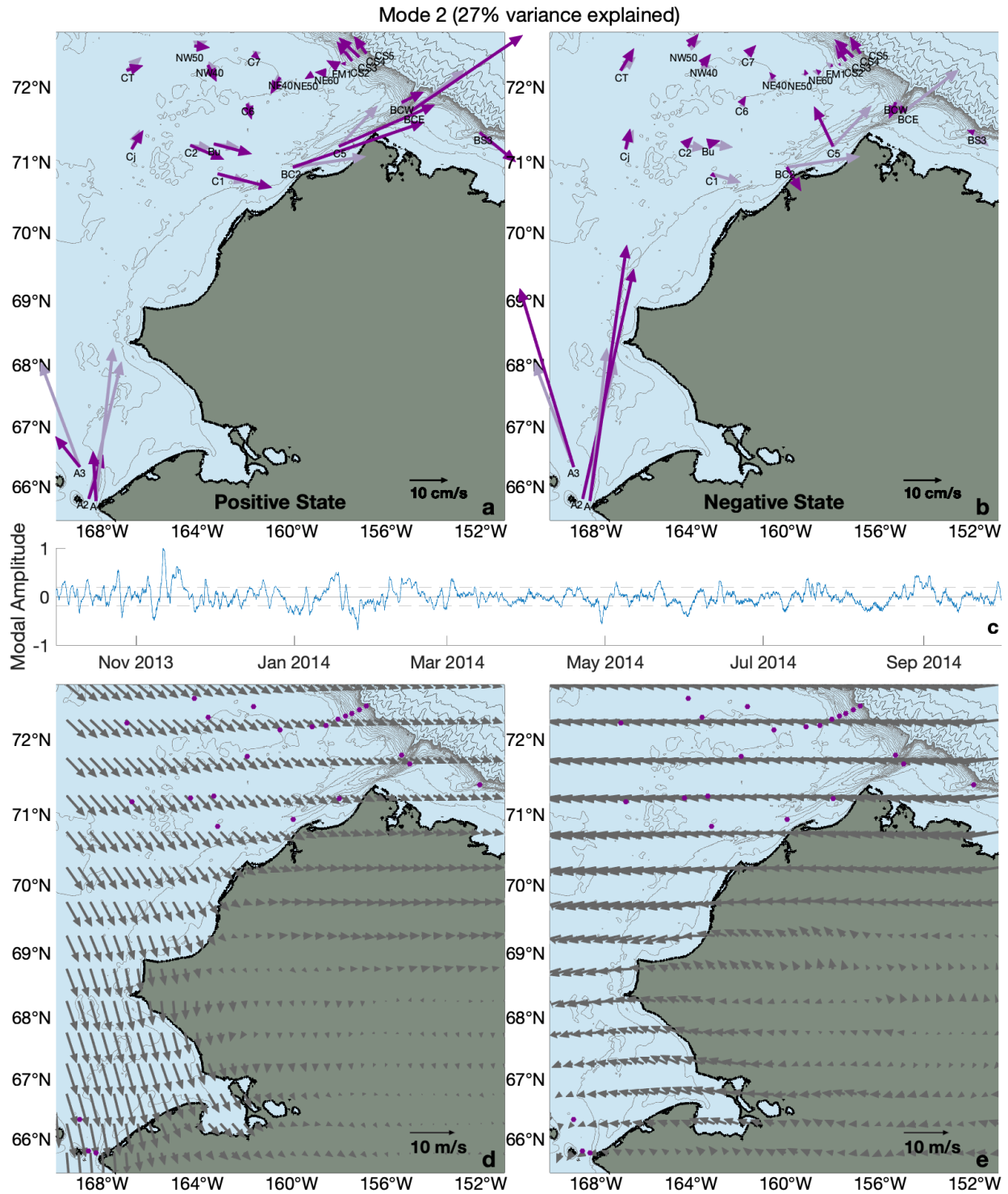
Figure 15. EOF mode 2 of mooring velocities (a) Mean velocities shown in light purple, structure function at +1 standard deviation added onto mean shown in dark purple. (b) Same as (a), but for -1 standard deviation. (c) Modal amplitude timeseries. (d) Composite ERA5 10 m wind field for all times when EOF mode 1 is above +1 standard deviation. The mooring locations are indicated by purple dots. (e) Same as (d), but for all times below -1 standard deviation.

34

762   composite also shows the dominance of northeasterly wind along the northwest coast of Alaska,

763   which accounts for the reversal of flow in Barrow Canyon (as shown in composites in section

764   4.1). Therefore, mode 1 describes coherent circulation across the Chukchi Sea when winds that

765   favor flow reversals in Barrow Canyon and Bering Strait are in phase with each other.

766   *6.3. Velocity EOF mode 2*

767   Mode 2, which explains 27% of the variability in the record, describes a less coherent

768   change in circulation across the shelf. We have again added the structure function at ±1 standard

769   deviation of the modal amplitude to the mean velocities at each mooring (Fig. 15a-b). Similar to

770   mode 1, the positive state is an enhancement of the mean flow across the northeastern Chukchi

771   Sea. However, the northward flow in Bering Strait is reduced, reminiscent of the negative state in

772   mode 1. Most moorings, including those east of Hanna Shoal, show velocity 1.5 to 2 times

773   greater than their mean, whereas velocities in Bering Strait are approximately one third of their

774   means. The negative state at 1 standard deviation shows enhanced northward flow in Bering

775   Strait (about 1.5 times greater than the mean) and weak flow in Barrow Canyon, upstream at C1,

776   and at BS3 on the Beaufort Slope. The rest of the moorings south and east of Hanna Shoal show

777   a slight decrease in velocities, while those north of Hanna Shoal show a slight increase.

778   Although the largest modal amplitude values for both the positive and negative states

779   occur in the winter, both frequently exceed one standard deviation throughout the year (Fig.

780   15c). Stronger cases of the positive state show a reversal of flow in Bering Strait (up to 2.5 times

781   the magnitude of the mean), and stronger cases of the negative state show a reversal of flow in

782   Barrow Canyon and across the rest of the shelf (up to 2-3 times the magnitude of the mean).

783   *6.4 Mode 2 relationship to regional wind*

784   We now consider the composite wind fields for all times when the modal amplitude

785   timeseries exceeded one standard deviation in each direction (Fig. 15d-e). When mode 2 is

786   higher than one standard deviation above the mean (13.6% of record), recall that flow is

787   enhanced relative to the mean circulation across most of the region, but reduced-to-reversed in

788   Bering Strait. The wind field composite (Fig. 15d) reveals a dominant northerly wind in Bering

789   Strait, accounting for the reduced-to-reversed flow there. The composite also shows the

790   dominance of northwesterly winds along the northwest coastline of Alaska, which, as noted

791   above, favors enhanced poleward flow in Barrow Canyon. Individual wind fields during these

792   times (not shown) reveal that wind actually varies from southwesterly to northeasterly,

793   converging on northwesterly as strength of the negative state increases.

794   When mode 2 is lower than one standard deviation below the mean (13.9% of record),

795   recall that flow is reduced relative to the mean across most of the shelf and weak-to-reversed in

796   Barrow Canyon, but enhanced in Bering Strait. The wind field composite (Fig. 15e) depicts very

797   weak wind in Bering Strait. Individual wind fields (not shown) reveal that both northerly and

798   southerly winds occur during these times. Northerly winds occur a higher proportion of the time,

799   but tend to be weaker. Northerly winds become less common in more extreme cases of the

800   negative state. Recall that the main driver of northward flow in Bering Strait is the Pacific-Arctic

801   pressure head, and that the mean winds (northerly) oppose this flow. Weak northerly winds,

802   therefore, result in northward flows above the annual mean. The wind composite reveals a

803   dominant easterly wind along the northwest coast of Alaska. Individual wind fields show that

804   wind direction can be easterly to northeasterly, with northeasterly more common in stronger

805   negative states. Therefore, mode 2 describes circulation during times when winds that favor flow

806   reversals in Barrow Canyon and Bering Strait are out of phase with each other.

807   In the positive state of mode 2, the reduced northward flow in Bering Strait combined

808   with enhanced down-canyon flow in Barrow Canyon would result in a divergence of flow

809   somewhere in the south or central Chukchi Sea. The opposite flow regime in the negative state

810   would result in a convergence of flow in the south or central Chukchi Sea. Weingartner et al.

811   (1998) also note periods of apparent flow convergence seen in monthly averages of mooring

812   velocities in Bering Strait, offshore of Cape Lisburne, and in upper Barrow Canyon. Without any

813   velocity moorings in the south or central Chukchi Sea, we are unable to explore this further.

814   However, Woodgate et al. (2005b) found a similar pair of EOF modes (using just the principal

815   component of velocity at each mooring). That study, conducted in 1990-91, consisted of twelve

816   moorings in three arrays: across Bering Strait, across the central Chukchi, and across the

817   northern Chukchi (with significant gaps). It was unusual in that it included moorings in the

818   western Chukchi (within the Russian EEZ), and offers us an interesting comparison. The

819   dominant mode in their EOF described coherent flow in Bering Strait, the central Chukchi, and

820   the northeastern Chukchi. Their second mode described times with opposing flow in different

821   parts of the Chukchi. The eastern half of the central line was coherent with the head of Barrow

822   Canyon, while the western half of the central line was coherent with Bering Strait and Long

823   Strait (far western Chukchi). While the Woodgate et al. moorings were placed more than two

824 decades prior to the moorings considered in this study, the similarity of the EOF analysis results

825 suggest that the occurrence of these two spatial patterns is typical for the region.

826 *6.5 Differences between flow regimes in modes 1 and 2*

827 So far, we have discussed Mode 1 and 2 in terms of flow reversals. However, there are

828 also differences in orientation of flow associated with each mode. To explore this, we will

829 compare the direction in which circulation is altered from the mean at the extremes of each

830 mode. The extremes are presented so as to maximize the contrast; one should bear in mind that

831 the differences are generally more subtle. The direction of change for the maximum states of the

832 two modes (Fig. 16a) allows us to see, under enhanced down-canyon flow in Barrow Canyon in

833
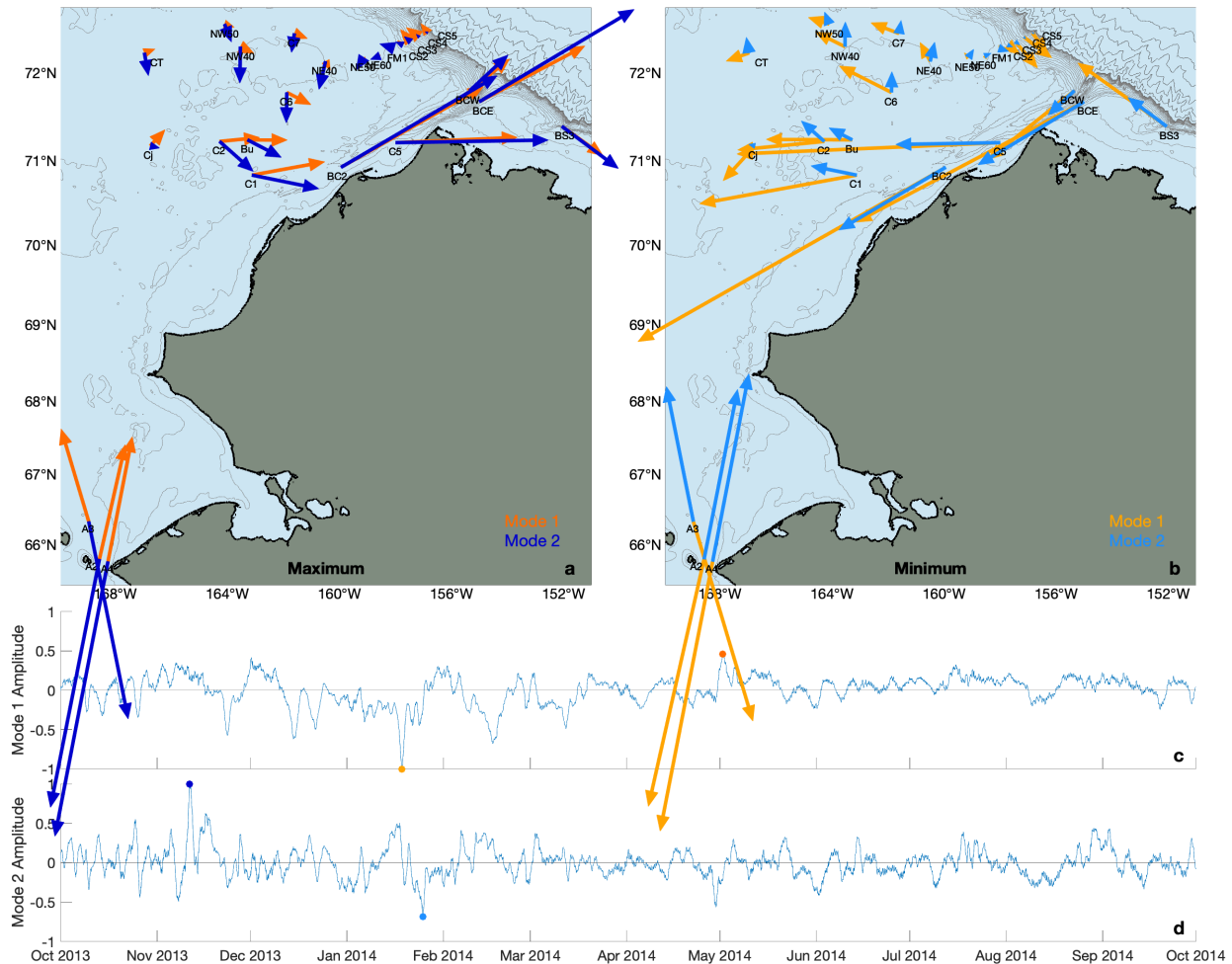
835 Figure 16. Relative change in flow direction associated with EOF modes 1 and 2 of mooring
836 velocities. (a) Change from mean velocity at maximum states. (b) Change from mean velocity at
837 minimum states. (c,d) Modal amplitude timeseries for each mode. The points in time depicted by
838 the mapped vectors are indicated by dots in the corresponding color.

839

840 both cases, the contrasting effects associated with northward and southward flow in Bering

841 Strait. As noted previously for the positive states, flow across the northeast Chukchi is generally

842 in the mean direction. However, southward flow in Bering Strait corresponds to a more

843 southward shift in orientation of flow at most mooring locations across the shelf. At the

844 minimum states of the two modes (Fig. 16b), flow in Barrow Canyon and across the shelf and

845 slope is reversed. In this case, northward flow in Bering Strait corresponds to a reversal of flow

846 across the shelf with a more northward shifted orientation. This shift in orientation does not

847 affect moorings in Barrow Canyon, on the Beaufort Slope, or on the Chukchi Slope, where flow

848 is more tightly bound to the bathymetry.

849

850 7. **Summary**

851   Through an expansive set of 27 moorings placed across the Chukchi Sea, adjacent slopes,

852 and in the Bering Strait from 2013-2014, we have been able to elucidate some of the controlling

853 factors of the synoptic-scale circulation. While the primary driver of northward flow into the

854 Chukchi Sea is the Pacific-Arctic pressure head, local winds have a strong influence over flow in

855 the region. The most dramatic effect of local wind forcing is the upwelling in Barrow Canyon,

856 which often draws both Pacific- and Atlantic-origin waters into the canyon. With several

857 moorings along the length of the canyon, this study revealed the progression of upwelled water.

858 Atlantic Water is frequently upwelled into Barrow Canyon in fall and winter, but is only

859 occasionally delivered onto the shelf. In order for Atlantic Water to make it as far as the head of

860 Barrow Canyon and onto the shelf, there must be a series of long upwelling events, with

861 insufficient time between events for the upwelled water to fully drain from the canyon.

862 Northeasterly wind is frequently implicated as the driver of these upwelling events. We find that

863 while the velocity response in Barrow Canyon generally increases with increasing wind event

864 strength, there are factors that complicate this relationship. These complications motivate further

865 study of additional forcing mechanisms.

866   The same northeasterly winds that force upwelling in Barrow Canyon also drive polynya

867 formation along the northwest coast of Alaska. However, polynyas in this region can also be

868 influenced by the upwelling. Warm waters transported into Barrow Canyon can melt sea ice and

869 enhance an existing polynya. This effect is especially dramatic when Atlantic Water is forced up

870 onto the shelf. An EOF analysis of ice cover during the full-ice period enabled us to gauge the

871   relative importance of wind-driven and sensible heat influences on polynyas in this area. The

872   results suggest a much larger spatial extent of warm water influence than has been previously

873   demonstrated. Our comparison with the local wind record also reveals a seasonally varying

874   relationship between wind and the polynya response. While a larger spatial scale EOF analysis of

875   ice cover mostly confirms the expected features of a seasonally ice-covered sea, it does provide a

876   useful illustration that consolidates these features into a compact form. It also reveals that freeze-

877   up occurs at a faster pace than melt-back and the inflow pathways have a similar spatial pattern

878   of influence on ice cover during both time periods.

879   An EOF analysis of 25 mooring velocity records revealed two distinct modes of

880   circulation. The first mode is associated with coherent flow across the region, with the positive

881   state corresponding to enhancement of mean circulation, and the negative state showing a

882   reversal of the mean circulation. The second mode describes times when flow in Barrow Canyon

883   and Bering Strait oppose each other, i.e. one is slowed or reversed while the other is enhanced.

884   Each state of the two modes is associated with a distinct regional wind pattern. Furthermore,

885   whether flow anomalies in Bering Strait and Barrow Canyon are coherent or oppose each other

886   has ramifications for flow across the rest of the shelf.

887   Quantifying the circulation of the Chukchi Sea and its relationship to wind and ice cover

888   is critical for improving our understanding of the regional ecosystem. One aspect of our results

889   that needs further explanation is the scatter in the relationship between wind event strength and

890   the velocity response in Barrow Canyon. We have speculated that this may be related to

891   northward propagating shelf waves originating in the Bering Sea, as suggested by Danielson et

892   al. (2014). Wind direction along the northwest coastline of Alaska is typically uniform, but some

893   of our data suggest that the times when it is not may be important in this regard. This is a topic of

894   on-going study using our composite timeseries.

904

905

906 **References**

907 Aagaard, K., & Roach, A. T. (1990). Arctic ocean-shelf exchange: Measurements in Barrow

908   Canyon. *Journal of Geophysical Research*, *95*(C10), 18163.

909   https://doi.org/10.1029/JC095iC10p18163

910 Beitsch, A., Kaleschke, L., & Kern, S. (2014). Investigating High-Resolution AMSR2 Sea Ice

911   Concentrations during the February 2013 Fracture Event in the Beaufort Sea. *Remote*

912   *Sensing*, *6*(5), 3841–3856. https://doi.org/10.3390/rs6053841

913 Bourke, R. H., & Paquette, R. G. (1976). Atlantic water on the Chukchi Shelf. *Geophysical*

914   *Research Letters*, *3*(10), 629–632. https://doi.org/10.1029/GL003i010p00629

915 Coachman, L. K., & Aagaard, K. (1966). On the water exchange through Bering Strait. *Limnology*

916   *and Oceanography*, *11*(1), 44–59. https://doi.org/10.4319/lo.1966.11.1.0044

917 Danielson, S. L., Weingartner, T. J., Hedstrom, K. S., Aagaard, K., Woodgate, R., Curchitser, E., &

918   Stabeno, P. J. (2014). Coupled wind-forced controls of the Bering–Chukchi shelf

919   circulation and the Bering Strait throughflow: Ekman transport, continental shelf waves,

920 and variations of the Pacific–Arctic sea surface height gradient. *Progress in*

921 *Oceanography*, *125*, 40–61. https://doi.org/10.1016/j.pocean.2014.04.006

922 Fang, Y., Weingartner, T. J., Dobbins, E. L., Winsor, P., Statscewich, H., Potter, R. A., Mudge, T.

923 D., Stoudt, C. A., & Borg, K. (2020). Circulation and Thermohaline Variability of the

924 Hanna Shoal Region on the Northeastern Chukchi Sea Shelf. *Journal of Geophysical*

925 *Research: Oceans*, *125*(7). https://doi.org/10.1029/2019JC015639

926 Frey, K. E., Moore, G. W. K., Cooper, L. W., & Grebmeier, J. M. (2015). Divergent patterns of

927 recent sea ice cover across the Bering, Chukchi, and Beaufort seas of the Pacific Arctic

928 Region. *Progress in Oceanography*, *136*, 32–49.

929 https://doi.org/10.1016/j.pocean.2015.05.009

930 Gong, D., & Pickart, R. S. (2016). Early summer water mass transformation in the eastern

931 Chukchi Sea. *Deep Sea Research Part II: Topical Studies in Oceanography*, *130*, 43–55.

932 https://doi.org/10.1016/j.dsr2.2016.04.015

933 Grebmeier, J. M., Cooper, L. W., Feder, H. M., & Sirenko, B. I. (2006). Ecosystem dynamics of the

934 Pacific-influenced Northern Bering and Chukchi Seas in the Amerasian Arctic. *Progress in*

935 *Oceanography*, *71*(2–4), 331–361. https://doi.org/10.1016/j.pocean.2006.10.001

936 Hirano, D., Fukamachi, Y., Ohshima, K. I., Watanabe, E., Mahoney, A. R., Eicken, H., Itoh, M.,

937 Simizu, D., Iwamoto, K., Jones, J., Takatsuka, T., Kikuchi, T., & Tamura, T. (2018). Winter

938 Water Formation in Coastal Polynyas of the Eastern Chukchi Shelf: Pacific and Atlantic

939 Influences. *Journal of Geophysical Research: Oceans*, *123*(8), 5688–5705.

940 https://doi.org/10.1029/2017JC013307

941   Hirano, D., Fukamachi, Y., Watanabe, E., Ohshima, K. I., Iwamoto, K., Mahoney, A. R., Eicken, H.,

942   Simizu, D., & Tamura, T. (2016). A wind-driven, hybrid latent and sensible heat coastal

943   polynya off Barrow, Alaska. *Journal of Geophysical Research: Oceans*, *121*(1), 980–997.

944   https://doi.org/10.1002/2015JC011318

945   Itoh, M., Nishino, S., Kawaguchi, Y., & Kikuchi, T. (2013). Barrow Canyon volume, heat, and

946   freshwater fluxes revealed by long-term mooring observations between 2000 and 2008:

947   BARROW CANYON FLUXES FOR 2000-2008. *Journal of Geophysical Research: Oceans*,

948   *118*(9), 4363–4379. https://doi.org/10.1002/jgrc.20290

949   Itoh, M., Shimada, K., Kamoshida, T., McLaughlin, F., Carmack, E., & Nishino, S. (2012).

950   Interannual variability of Pacific Winter Water inflow through Barrow Canyon from 2000

951   to 2006. *Journal of Oceanography*, *68*(4), 575–592. https://doi.org/10.1007/s10872-

952   012-0120-1

953   Ladd, C., Mordy, C. W., Salo, S. A., & Stabeno, P. J. (2016). Winter Water Properties and the

954   Chukchi Polynya: WATER PROPERTIES AND CHUKCHI POLYNYA. *Journal of Geophysical*

955   *Research: Oceans*, *121*(8), 5516–5534. https://doi.org/10.1002/2016JC011918

956   Li, M., Pickart, R. S., Spall, M. A., Weingartner, T. J., Lin, P., Moore, G. W. K., & Qi, Y. (2019).

957   Circulation of the Chukchi Sea shelfbreak and slope from moored timeseries. *Progress in*

958   *Oceanography*, *172*, 14–33. https://doi.org/10.1016/j.pocean.2019.01.002

959   Lin, P., Pickart, R. S., McRaven, L. T., Arrigo, K. R., Bahr, F., Lowry, K. E., Stockwell, D. A., &

960   Mordy, C. W. (2019). Water Mass Evolution and Circulation of the Northeastern Chukchi

961   Sea in Summer: Implications for Nutrient Distributions. *Journal of Geophysical Research:*

962   *Oceans*, *124*(7), 4416–4432. https://doi.org/10.1029/2019JC015185

963   Lin, P., Pickart, R. S., Moore, G. W. K., Spall, M. A., & Hu, J. (2019). Characteristics and dynamics

964   of wind-driven upwelling in the Alaskan Beaufort Sea based on six years of mooring

965   data. *Deep Sea Research Part II: Topical Studies in Oceanography*, *162*, 79–92.

966   https://doi.org/10.1016/j.dsr2.2018.01.002

967   Lin, P., Pickart, R. S., Stafford, K. M., Moore, G. W. K., Torres, D. J., Bahr, F., & Hu, J. (2016).

968   Seasonal variation of the Beaufort shelfbreak jet and its relationship to Arctic cetacean

969   occurrence: SEASONAL VARIATION OF THE BEAUFORT JET. *Journal of Geophysical*

970   *Research: Oceans*, *121*(12), 8434–8454. https://doi.org/10.1002/2016JC011890

971   Moore, S. E., & Stabeno, P. J. (2015). Synthesis of Arctic Research (SOAR) in marine ecosystems

972   of the Pacific Arctic. *Progress in Oceanography*, *136*, 1–11.

973   https://doi.org/10.1016/j.pocean.2015.05.017

974   Morales Maqueda, M. A. (2004). Polynya Dynamics: A Review of Observations and Modeling.

975   *Reviews of Geophysics*, *42*(1), RG1004. https://doi.org/10.1029/2002RG000116

976   Nikolopoulos, A., Pickart, R. S., Fratantoni, P. S., Shimada, K., Torres, D. J., & Jones, E. P. (2009).

977   The western Arctic boundary current at 152°W: Structure, variability, and transport.

978   *Deep Sea Research Part II: Topical Studies in Oceanography*, *56*(17), 1164–1181.

979   https://doi.org/10.1016/j.dsr2.2008.10.014

980   Pacini, A., Moore, G. W. K., Pickart, R. S., Nobre, C., Bahr, F., Våge, K., & Arrigo, K. R. (2019).

981   Characteristics and Transformation of Pacific Winter Water on the Chukchi Sea Shelf in

982   Late Spring. *Journal of Geophysical Research: Oceans*, *124*(10), 7153–7177.

983   https://doi.org/10.1029/2019JC015261

984   Pawlowicz, R., Beardsley, B., & Lentz, S. (2002). Classical tidal harmonic analysis including error

985   estimates in MATLAB using T_TIDE. *Computers & Geosciences*, *28*(8), 929–937.

986   https://doi.org/10.1016/S0098-3004(02)00013-4

987   Pickart, R. S., Moore, G. W. K., Mao, C., Bahr, F., Nobre, C., & Weingartner, T. J. (2016).

988   Circulation of winter water on the Chukchi shelf in early Summer. *Deep Sea Research*

989   *Part II: Topical Studies in Oceanography*, *130*, 56–75.

990   https://doi.org/10.1016/j.dsr2.2016.05.001

991   Pickart, R. S., Nobre, C., Lin, P., Arrigo, K. R., Ashjian, C. J., Berchok, C., Cooper, L. W.,

992   Grebmeier, J. M., Hartwell, I., He, J., Itoh, M., Kikuchi, T., Nishino, S., & Vagle, S. (2019).

993   Seasonal to mesoscale variability of water masses and atmospheric conditions in Barrow

994   Canyon, Chukchi Sea. *Deep Sea Research Part II: Topical Studies in Oceanography*, *162*,

995   32–49. https://doi.org/10.1016/j.dsr2.2019.02.003

996   Pickart, R. S., Schulze, L. M., Moore, G. W. K., Charette, M. A., Arrigo, K. R., van Dijken, G., &

997   Danielson, S. L. (2013). Long-term trends of upwelling and impacts on primary

998   productivity in the Alaskan Beaufort Sea. *Deep Sea Research Part I: Oceanographic*

999   *Research Papers*, *79*, 106–121. https://doi.org/10.1016/j.dsr.2013.05.003

1000   Pisareva, M. N., Pickart, R. S., Lin, P., Fratantoni, P. S., & Weingartner, T. J. (2019). On the nature

1001   of wind-forced upwelling in Barrow Canyon. *Deep Sea Research Part II: Topical Studies in*

1002   *Oceanography*, *162*, 63–78. https://doi.org/10.1016/j.dsr2.2019.02.002

1003   Serreze, M. C., Crawford, A. D., Stroeve, J. C., Barrett, A. P., & Woodgate, R. A. (2016).

1004   Variability, trends, and predictability of seasonal sea ice retreat and advance in the

1005   Chukchi Sea: SEA ICE IN THE CHUKCHI SEA. *Journal of Geophysical Research: Oceans*,

1006   *121*(10), 7308–7325. https://doi.org/10.1002/2016JC011977

1007   Spall, M. A. (2007). Circulation and water mass transformation in a model of the Chukchi Sea.

1008   *Journal of Geophysical Research*, *112*(C5), C05025.

1009   https://doi.org/10.1029/2005JC003364

1010   Spreen, G., Kaleschke, L., & Heygster, G. (2008). Sea ice remote sensing using AMSR-E 89-GHz

1011   channels. *Journal of Geophysical Research*, *113*(C2), C02S03.

1012   https://doi.org/10.1029/2005JC003384

1013   Tian, F., Pickart, R. S., Lin, P., Pacini, A., Moore, G. W. K., Stabeno, P., Weingartner, T., Itoh, M.,

1014   Kikuchi, T., Dobbins, E., Bell, S., Woodgate, R. A., Danielson, S. L., & Wang, Z. (2021).

1015   Mean and Seasonal Circulation of the Eastern Chukchi Sea From Moored Timeseries in

1016   2013–2014. *Journal of Geophysical Research: Oceans*, *126*(5).

1017   https://doi.org/10.1029/2020JC016863

1018   Weingartner, T. J., Cavalieri, D. J., Aagaard, K., & Sasaki, Y. (1998). Circulation, dense water

1019   formation, and outflow on the northeast Chukchi Shelf. *Journal of Geophysical Research:*

1020   *Oceans*, *103*(C4), 7647–7661. https://doi.org/10.1029/98JC00374

1021   Woodgate, R. (2012). *Arctic Ocean Circulation – going around at the top of the world*. 15.

1022   Woodgate, R. A. (2018). Increases in the Pacific inflow to the Arctic from 1990 to 2015, and

1023   insights into seasonal trends and driving mechanisms from year-round Bering Strait

1024   mooring data. *Progress in Oceanography*, *160*, 124–154.

1025   https://doi.org/10.1016/j.pocean.2017.12.007

1026   Woodgate, R. A., Aagaard, K., & Weingartner, T. J. (2005a). Monthly temperature, salinity, and

1027   transport variability of the Bering Strait through flow: BERING STRAIT THROUGH FLOW.

1028   *Geophysical Research Letters*, *32*(4), n/a-n/a. https://doi.org/10.1029/2004GL021880

1029   Woodgate, R. A., Aagaard, K., & Weingartner, T. J. (2005b). A year in the physical oceanography

1030   of the Chukchi Sea: Moored measurements from autumn 1990–1991. *Deep Sea*

1031   *Research Part II: Topical Studies in Oceanography*, *52*(24–26), 3116–3149.

1032   https://doi.org/10.1016/j.dsr2.2005.10.016

1033   Woodgate, R. A., Weingartner, T., & Lindsay, R. (2010). The 2007 Bering Strait oceanic heat flux

1034   and anomalous Arctic sea-ice retreat: 2007 BERING STRAIT OCEANIC HEAT FLUX.

1035   *Geophysical Research Letters*, *37*(1), n/a-n/a. https://doi.org/10.1029/2009GL041621

1036   Woodgate, R., Stafford, K., & Prahl, F. (2015). A Synthesis of Year-Round Interdisciplinary

1037   Mooring Measurements in the Bering Strait (1990–2014) and the RUSALCA Years (2004–

1038   2011). *Oceanography*, *28*(3), 46–67. https://doi.org/10.5670/oceanog.2015.57

1039